

Bio-optical characterization of subsurface chlorophyll maxima in the Mediterranean Sea from a Biogeochemical-Argo float database

Marie Barbioux¹, Julia Uitz¹, Bernard Gentili¹, Orens Pasqueron de Fommervault², Alexandre Mignot³, Antoine Poteau¹, Catherine Schmechtig⁴, Vincent Taillandier¹, Edouard Leymarie¹, Christophe Penker'h¹, Fabrizio D'Ortenzio¹, Hervé Claustre¹ & Annick Bricaud¹

¹CNRS and Sorbonne Université, Laboratoire d'Océanographie de Villefranche, LOV, F-06230 Villefranche-sur-mer, France

²Alseamar-alcen company, 9 Europarc Sainte Victoire, 13590 Meyreuil, France

³Mercator Océan, 31520 Ramonville Saint Agne

⁴OSU Ecce Terra, UMS 3455, CNRS and Sorbonne Université, Paris 6, 4 place Jussieu 75252 Paris cedex 05, France

Correspondence to: Marie Barbioux (marie.barbioux@obs-vlfr.fr)

ABSTRACT

As commonly observed in oligotrophic stratified waters, a Subsurface (or Deep) Chlorophyll Maximum (SCM) frequently characterizes the vertical distribution of phytoplankton chlorophyll in the Mediterranean Sea. Occurring far from the surface layer “seen” by ocean color satellites, SCMs are difficult to observe with adequate spatio-temporal resolution and their biogeochemical impact remains unknown. BioGeochemical-Argo (BGC-Argo) profiling floats represent appropriate tools for studying the dynamics of SCMs. Based on data collected from 36 BGC-Argo floats deployed in the Mediterranean Sea, our study aims to address two main questions: (1) What are the different types of SCMs in Mediterranean Sea? (2) Which environmental factors control their occurrence and dynamics? First, we analyzed the seasonal and regional variations of the chlorophyll concentration (Chl_a), particulate backscattering coefficient (b_{bp}), a proxy of the Particulate Organic Carbon (POC), and environmental parameters (PAR and nitrates) within the SCM layer over the Mediterranean basin. The vertical profiles of Chl_a and b_{bp} were then statistically classified, and the seasonal occurrence of each of the different types of SCMs quantified. Finally, a case study was performed on two contrasted regions and the environmental conditions at depth were further investigated to understand the main controls on the SCMs. In the Eastern Basin, SCMs result, at a first order, from photoacclimation process. Conversely, SCMs in the Western Basin reflect a biomass increase at depth benefiting from both light and nitrate resources. Our results also suggest that a variety of intermediate types of SCMs are encountered between these two end-member situations.

34 1 INTRODUCTION

35 The vertical distribution of phytoplankton in the open ocean is often characterized by
36 the occurrence of high chlorophyll *a* concentration (Chl*a*) beneath the mixed layer (Cullen
37 and Eppley, 1981; Fasham et al., 1985; Raimbault et al., 1993; Letelier et al., 2004; Tripathy
38 et al., 2015). This phenomenon is commonly referred to as Deep Chlorophyll Maximum
39 (DCM) or Subsurface Chlorophyll Maximum (SCM). Although it always happens below the
40 surface layer (approximately below the first 20 meters), it does not necessarily settle very
41 deep in the water column, thus making the notation DCM sometimes inappropriate. Hence, in
42 the following, we will use the notation SCM. Commonly observed at depth in oligotrophic
43 stratified regions (Anderson, 1969; Cullen, 1982; Furuya, 1990; Mignot et al., 2014), SCMs
44 are also known to occur below the mixed layer in temperate- and high-latitude environments
45 (Parslow et al., 2001; Uitz et al., 2009; Ardyna et al., 2013; Arrigo et al., 2011). The
46 formation of a subsurface maximum of Chl*a* in these different ecosystems results from
47 various underlying mechanisms leading to different types of SCMs. In stratified waters,
48 SCMs often result from photoacclimation of the phytoplankton organisms, which induces an
49 increase in the intracellular Chl*a* in response to low light conditions (Kiefer et al., 1976; Winn
50 et al., 1995; Fennel and Boss, 2003; Dubinsky and Stambler, 2009). However SCMs resulting
51 from an actual increase in phytoplankton carbon biomass have also been reported in such
52 ecosystems (Beckmann and Hense, 2007; Crombet et al., 2011; Mignot et al., 2014). In high-
53 latitude regions with well-mixed surface waters, SCMs have been shown to result from the
54 accumulation of particles sinking from the mixed layer (Quéguiner et al., 1997; Parslow et al.,
55 2001), photophysiological acclimation of algal cells (Mikaelyan and Belyaeva, 1995) or
56 phytoplankton growth at the depth of the nutricline (Holm-Hansen and Hewes, 2004; Tripathy
57 et al., 2015). Hence, regional or local studies have highlighted underlying processes indicating
58 that, under certain conditions, SCMs could contribute to carbon production and export, and

59 thus potentially have an important biogeochemical role. However, we have limited knowledge
60 of their biogeochemical significance at large spatial and temporal scales. Their contribution to
61 the depth-integrated primary production has been assessed for a limited number of regions
62 and remains largely unknown. It has been reported to be underestimated from 40 to 75% in
63 the Arctic Ocean (Ardyna et al., 2013; Hill et al., 2013), to more than 40% in the oligotrophic
64 Atlantic (Perez et al., 2006), 40–50% in the Celtic Sea (Hickman et al., 2012) and about 58%
65 in the North Sea (Weston et al., 2005). The biogeochemical contribution of the SCMs to the
66 global ocean is also particularly hard to assess at large spatio-temporal scales, especially
67 because SCMs settle at a depth usually far from the surface layer “seen” by ocean color
68 satellites. Remotely sensed estimates are restricted to the upper layer of the water column that
69 represent only one fifth of the euphotic layer where phytoplankton photosynthesis takes place
70 (Gordon and McCluney, 1975). The exact biogeochemical role of SCMs, thus, needs to be
71 further explored.

72 The Mediterranean Sea is considered as an oligotrophic province where the vertical
73 distribution of phytoplankton is, seasonally or permanently, characterized by the occurrence
74 of a SCM (Kimor et al., 1987; Estrada et al., 1993; Videau et al., 1994; Christaki et al., 2001;
75 Siokou-Frangou et al., 2010; Lavigne et al., 2015). It is also a low-nutrient concentration
76 basin, one of the largest nutrient-depleted areas of the global ocean and it is characterized by a
77 west-to-east gradient in both nutrients and **Chl a** (Dugdale and Wilkerson, 1988; Bethoux et
78 al., 1992; Antoine et al., 1995; Bosc et al., 2004; D’Ortenzio and Ribera d’Alcalà, 2009).
79 While the Eastern Basin is defined as oligotrophic (Krom et al., 1991; Ignatiades et al., 2002;
80 Lavigne et al., 2015), the Western Basin is more productive and behaves as a temperate
81 system (Morel and André, 1991; Marty et al., 2002; Mayot et al., 2017b). Hence, this
82 “miniature ocean” presents SCMs that may be encountered in both seasonally stratified
83 environments and permanently stratified waters of the global ocean. This, coupled with an

84 intensive effort of biogeochemical observations in this region, makes the Mediterranean Sea
85 an ideal region for studying SCMs.

86 The biogeochemical and bio-optical community recently developed autonomous
87 profiling floats that collect *in situ* vertical profiles of biogeochemical properties such as the
88 chlorophyll *a* fluorescence (*i.e.* a proxy of the **Chl*a***) and the particulate backscattering
89 coefficient (b_{bp}) (*i.e.* a proxy of the Particulate Organic Carbon (POC)). Physical-chemical
90 properties such as nitrate concentration ($[NO_3^-]$) or the Photosynthetically Available Radiation
91 (PAR), essential to understand the functioning of SCMs, are also measured simultaneously
92 (Johnson et al., 2009; Claustre et al., 2010; Johnson and Claustre, 2016). Thirty-six
93 BioGeochemical-Argo (BGC-Argo) have been deployed in the Mediterranean Sea from 2012
94 to 2017, providing a database of 4050 *in situ* multi-variable profiles. This extensive database
95 gives us the unique opportunity to enhance our comprehension of the vertical distribution and
96 seasonal variability of the phytoplankton biomass in the subsurface layer of the Mediterranean
97 Sea and expand our understanding of the mechanisms involved in the occurrence of SCMs.
98 Our study seeks to address two main questions: (1) **what** are the different types of SCMs in
99 Mediterranean Sea?; and (2) **which** environmental factors control the occurrence and
100 dynamics of the different types of SCMs in this region? To address these questions, three
101 complementary approaches were used. First, based on a climatological approach, we analyzed
102 the spatial and seasonal variability of biogeochemical properties (*i.e.* Chl*a* and b_{bp}) and
103 environmental conditions at the SCM level. This should lead to the identification of the main
104 mechanisms controlling SCMs in different regions of the Med Sea. Second, using a statistical
105 method, we classified the vertical profiles of Chl*a* and b_{bp} seasonally encountered in the
106 various regions of the **Mediterranean Sea**. This approach allowed us to quantify the frequency
107 of occurrence of distinct types of SCMs in these different regions. Finally, using two specific
108 BGC-Argo floats deployed in the Gulf of Lions and the Levantine Sea, we conducted a case

109 study of two contrasted regimes and investigate the environmental conditions that control the
110 occurrence of SCMs in each regime.

111 **2 DATA AND METHODS**

112 **2.1 The BGC-Argo profiling float database**

113 Thirty-six BGC-Argo profiling floats were deployed in the Mediterranean Sea in 5
114 geographic areas, *i.e.* the Northwestern (NW) and Southwestern (SW) regions, the Tyrrhenian
115 (TYR), Ionian (ION) and Levantine (LEV) Seas. Our study was based on the analysis of a
116 database comprising 4050 multivariable vertical profiles, corresponding to upward casts
117 collected between November 26, 2012 and September 27, 2017 (Table 1 and Figure 1). The
118 “PROVOR CTS-4” (NKE Marine Electronics, Inc.) is a profiling autonomous platform that
119 has been specifically designed in the frame of the remOcean and NAOS projects. The
120 physical variables (depth, temperature and salinity) were acquired by a SBE 41 CTD (Sea-
121 Bird Scientific Inc.). Two optical packages, the so-called remA and remB, were developed to
122 be specifically implemented on profiling floats. The remA is composed of an OCR-504
123 (SAtlantic, Inc.), a multispectral radiometer that measures the Photosynthetically Available
124 Radiation (PAR) and the downwelling irradiance at 380, 410 and 490 nm. The remA also
125 includes an ECO3 sensor (Combined Three Channel Sensors; WET Labs, Inc.) measuring the
126 fluorescence of the chlorophyll *a* and the Colored Dissolved Organic Matter (CDOM) at
127 excitation/emission wavelengths of 470/695 nm and 370/460 nm, respectively, and the
128 angular scattering coefficient of particles ($\beta(\theta, \lambda)$) at 700 nm and at an angle of 124°. Finally,
129 15 floats were also equipped with a nitrate (NO_3^-) (Deep SUNA, Sea-Bird Scientific, Inc.)
130 or/and an oxygen (O_2) sensor (optode 4330, Aanderaa, Inc.). Depending on the scientific
131 objectives of the different projects, the measurements were collected during upward casts
132 programmed every 1, 2, 3, 5, or 10 days. All casts started from a parking depth at 1000 m at a

133 time that was sufficient for surfacing around local noon. The vertical resolution of data
134 acquisition was 10 m between 1000 m and 250 m, 1 m between 250 m and 10 m, and 0.2 m
135 between 10 m and the surface. Each time the floats surfaced, the raw data were transmitted to
136 land through Iridium two-way communication.

137 **2.2 Retrieval of key biogeochemical variables from optical measurements**

138 For each bio-optical parameter, raw counts were converted into the desired quantities
139 according to technical specifications and calibration coefficients provided by the
140 manufacturer. These quantities were transformed into **Chla** and particulate backscattering
141 coefficient (b_{bp}) following the BGC-Argo procedure (Schmechtig et al., 2015, 2016b;
142 Organelli et al., 2017b). This procedure included a correction of non-photochemical
143 quenching for Chla following Xing et al. (2012) method. In addition, we applied a correction
144 factor to Chla fluorescence measurements from the BGC-Argo floats, following the
145 recommendation of Roesler et al. (2017). Comparing estimates of Chla from the WET Labs
146 ECO fluorometers (used on BGC-Argo floats) with Chla estimates from other methods, these
147 authors evidenced a bias varying according to the region sampled. In order to quantify this
148 bias, they calculated the slope of the relationship between the Chla values from the ECO
149 fluorometers and those estimated independently using HPLC analyses. This bias was further
150 confirmed using optical proxies such as *in situ* radiometric measurements (Xing et al., 2011)
151 or algal absorption measurements (Boss et al., 2013; Roesler and Barnard, 2013). At a global
152 scale, Roesler et al. (2017) evidenced an overestimation of the Chla concentration by a factor
153 of 2, on which regional variations of the fluorescence-to-Chla ratio are superimposed. This
154 correction factor applied to BGC-Argo data was found to have little impact on the
155 interpretation of the results on a global scale (Barbieux et al., 2017; Organelli et al., 2017a)
156 and did not modify the interpretation of the present results, especially because the regional
157 correction factors proposed by Roesler et al. (2017) for the Mediterranean Sea are very close

158 to the global factor of 2 (1.62 and 1.72 for the Western and Eastern Basin, respectively).
159 Finally a quality-controlled procedure was performed following the BGC-Argo
160 recommendations (Schmechtig et al., 2016a). All data were also visually checked in order to
161 detect any drift over time or sensor deficiency. These data were made freely available by the
162 International Argo Program (<http://www.argo.ucsd.edu>, <http://argo.jcommops.org>) and the
163 CORIOLIS project (<http://www.coriolis.eu.org>).

164 After binning the data at a 1-m resolution, the mixed layer depth (MLD) was derived
165 from the CTD data using the density criterion of de Boyer Montégut (2004). The MLD was
166 calculated as the depth where the density difference compared to the surface (10 m) reference
167 value is 0.03 kg m^{-3} . The depth of the SCM and of the Subsurface b_{bp} Maximum ($Sb_{bp}M$) was
168 identified as the depth where the absolute value of $Chla$ or b_{bp} reaches a maximum below the
169 MLD. Large spikes associated with particle aggregates or zooplankton (Gardner et al., 2000;
170 Briggs et al., 2011) were observed in the b_{bp} profiles and made it sometimes difficult to
171 identify the depth of the $Sb_{bp}M$. Hence, for the purpose of the $Sb_{bp}M$ retrieval exclusively, the
172 b_{bp} values were smoothed with a mean filter (5-point window). To study the SCM dynamics
173 and obtain the width of the SCM that may fluctuate in space and time, a Gaussian profile was
174 adjusted to each $Chla$ vertical profile of the database that presented a SCM. This approach
175 first proposed by Lewis et al. (1983) has been widely used in oceanographic studies (e.g.
176 Morel and Berthon, 1989; Uitz et al., 2006; Barbieux et al., 2017). The width of the gaussian
177 adjusted to the vertical profile of $Chla$ represented the width of the SCM. The SCM layer was
178 defined as the layer extending across the entire width of the SCM. The upper (or lower) limit
179 was retrieved by removing (or adding) half of the width of the SCM to the absolute depth of
180 the SCM.

181 2.3 Estimation of nitrate concentration

182 The SUNA sensor measures the light absorption in the wavelength range from 217 to
183 240 nm. In this spectral band, the light absorption is dominated by nitrates and bromides, and,
184 to a much lesser extent, by organic matter (Johnson and Coletti, 2002). Various algorithms
185 were developed to obtain the nitrate concentration ($[\text{NO}_3^-]$) from the measured light
186 absorption spectrum (*e.g.* Arai et al., 2008; Zielinski et al., 2011). The TCSS algorithm was
187 specifically developed to take into account the temperature dependency of the bromide
188 spectrum, which significantly improved the accuracy of the retrieved $[\text{NO}_3^-]$ (Sakamoto et al.,
189 2009). This algorithm was recently modified to also take into account a pressure dependency
190 (Pasqueron de Fommervault et al., 2015a; Sakamoto et al., 2017). Previous studies also
191 evidenced the inaccuracy of standard calibration procedures (D'Ortenzio et al., 2014;
192 Pasqueron de Fommervault et al., 2015a) and showed that SUNA sensors often undergo offset
193 issue and drift over time (Johnson and Coletti, 2002). Johnson et al. (2017) proposed a
194 method to correct these issues for the Southern Ocean. Using the GLODAP-V2 database
195 (<http://cdiac.ornl.gov/oceans/GLODAPv2>) of *in situ* measurements, the authors determined an
196 empirical relationship allowing the estimation of the $[\text{NO}_3^-]$ at depth ($[\text{NO}_3^-]_{\text{deep_pred}}$ for
197 nitrate concentration deep reference value) using a multiple linear regression (MLR) with
198 physical and geolocation parameters as predictors (salinity, temperature, oxygen, latitude and
199 longitude). BGC-Argo profiles of nitrate concentration were then corrected by adjusting the
200 SUNA measurements to the retrieved deep reference value. Following a similar approach, we
201 established a regional empirical relationship for the Mediterranean Sea (Eq.1) allowing to
202 retrieve the $[\text{NO}_3^-]_{\text{deep_pred}}$ values using parameters that were systematically measured by
203 the BGC-Argo floats (*i.e.* latitude, longitude, temperature and salinity). For the Mediterranean
204 Sea, oxygen was not used as an input parameter of the MLR as this parameter was not

205 systematically available for the BGC-Argo floats of our database. Moreover, its absence in
206 the MLR as an input parameter did not affect the retrieval of the nitrate concentrations.
207 Comparing the nitrate concentrations predicted by the MLR to the nitrate concentrations from
208 GLODAP-V2 data, the determination coefficients of the relationship presented very similar
209 values for the model with and without oxygen (see Figure S1 in Supplement 1).

210 Hence, the following equation was finally used:

$$211 \quad [\text{NO}_3^-]_{\text{deep_pred}} = 454.28 - 0.002 \times \text{Latitude} - 0.0473 \times \text{Longitude} + 1.7262 \times \text{Temperature} - \\ 212 \quad 12.165 \times \text{Salinity} \quad (1)$$

213 A strong correlation was noticed between the nitrate concentrations predicted from the MLR
214 model and the measurements provided in the GLODAP-V2 database. This correlation was
215 associated with a strong determination coefficient ($R^2 = 0.89$) and a small root mean square
216 error ($\text{RMSE} = 0.52 \mu\text{mol L}^{-1}$). Then, comparing the predicted climatology-based with the
217 observed BGC-Argo nitrate concentrations at depth and computing the adjusted nitrate
218 concentration for each depth, we obtained the following equation:

$$219 \quad [\text{NO}_3^-]_{\text{adjusted}}(t,z) = [\text{NO}_3^-]_{\text{raw}}(t,z) - ([\text{NO}_3^-]_{\text{deep_obs}}(t) - [\text{NO}_3^-]_{\text{deep_pred}}(t)) \quad (2)$$

220 with $[\text{NO}_3^-]_{\text{raw}}(t,z)$ corresponding to the raw nitrate value from the SUNA sensor.

221 The BGC-Argo $[\text{NO}_3^-]$ profiles of the Mediterranean database were compared with *in*
222 *situ* measurements collected simultaneously to float deployment (see Taillandier et al., 2017
223 for more details), using the classic colorimetric method (Morris and Riley, 1963). We
224 demonstrated that the retrieval of the BGC-Argo $[\text{NO}_3^-]$ with the proposed calibration
225 procedure was satisfying. The comparison between the nitrate concentrations retrieved from
226 the BGC-Argo floats to the reference *in situ* measurements (Figure 2) showed a robust
227 relationship ($R^2 = 0.86$ and slope = 0.97, $N = 162$).

228 The nitracline that separates upper nitrate-depleted waters from lower repleted waters
 229 corresponds, in this paper, to the depth where $[\text{NO}_3^-]$ is $1 \mu\text{M}$ smaller than the median $[\text{NO}_3^-]$
 230 value in the first 10 meters of the water column (Lavigne et al., 2013). The diffusive vertical
 231 supply of nitrates to the euphotic zone is not only influenced by the depth of the nitracline
 232 from the sunlit surface layer but also by the slope of the nitracline. The slope of the nitracline
 233 was calculated as the vertical $[\text{NO}_3^-]$ gradient between the isocline $1 \mu\text{M}$ and the isocline 3
 234 μM as already done for the Mediterranean Sea by Pasqueron de Fommervault et al. (2015a).

235 **2.4 Estimation of daily PAR**

236 The BGC-Argo vertical profiles of PAR were quality-checked following Organelli et al.
 237 (2016). Only solar noon profiles were considered for our analysis because zenith
 238 measurements ensure the best retrieval (Organelli et al., 2017) of the isolume, *i.e.* depth
 239 corresponding to a chosen value of light. BGC-Argo floats provide instantaneous PAR
 240 (iPAR) measurements just beneath the sea surface at local noon (iPAR(0^- , noon)).

241 From iPAR measurement, a vertical profile of daily-averaged PAR was estimated
 242 following the method of Mignot et al. (2018). This method relies on a theoretical clear-sky
 243 estimate of iPAR just beneath the sea surface using the solar irradiance model SOLPOS
 244 developed by the National Renewable Energy Laboratory (NREL, 2000). Hence, we followed
 245 three main steps:

246 (1) The instantaneous photosynthetically available radiation just beneath the sea surface at
 247 time t , iPAR(0^- , t) in $\mu\text{mol photons m}^{-2} \text{s}^{-1}$, was determined from Eq. (3):

$$248 \text{iPAR}(0^-, t) = \text{iPAR}_{\text{clear}}(0^-, t) \frac{\text{iPAR}(0^-, \text{noon})}{\text{iPAR}_{\text{clear}}(0^-, \text{noon})} \quad (3)$$

249 with $\text{iPAR}_{\text{clear}}(0^-, t)$ the theoretical estimate of iPAR just beneath the sea surface at time t ,
 250 $\text{iPAR}(0^-, \text{noon})$ the float measurement of iPAR just beneath the sea surface at local noon,

251 and $iPAR_{clear}(0^-, noon)$ the theoretical estimate of $iPAR$ just beneath the sea surface at local
 252 noon for the same time and location as the float measurement. The ratio of $iPAR(0^-, noon)$ to
 253 $iPAR_{clear}(0^-, noon)$ represented an index of the cloud coverage at noon, which was applied
 254 to the clear-sky $iPAR$ estimates at any time t . This approach thus assumes that the cloud
 255 coverage at noon is representative of the daily cloud coverage. Although the cloud coverage is
 256 unlikely to be constant throughout the entire day, this approach enabled to account for the
 257 daily course of light through modeled estimates, rather than considering only the noon-time
 258 instantaneous float measurements.

259 (2) The daily-averaged PAR just beneath sea surface, $PAR(0^-)$ in $mol\ photons\ m^{-2}\ d^{-1}$, was
 260 obtained by averaging Eq. (3) over daylength. In parallel, the diffuse attenuation coefficient
 261 for PAR , $K_d(PAR)$ in unit of m^{-1} , was derived from the float $iPAR$ measurements by fitting a
 262 linear least square regression forced through the origin between the data of
 263 $\ln\left(\frac{iPAR_{float}(z, noon)}{iPAR_{float}(0^-, noon)}\right)$ and z taken in the upper 40 m of the water column (Mignot et al.,
 264 2018).

265 (3) Finally, the daily-averaged PAR for each depth z of the water column, $PAR(z)$ in units of
 266 $mol\ photons\ m^{-2}\ d^{-1}$, was calculated from $K_d(PAR)$ and $PAR(0^-)$ as follows:

$$267 \quad PAR(z) = PAR(0^-) \exp(K_d(PAR)z) \quad (4)$$

268 Additionally, the isolume $0.3\ mol\ quanta.m^{-2}\ d^{-1}$, which corresponds to the dataset
 269 median daily PAR value at the SCM depth, was used as an indicator of the light available for
 270 photosynthesis at the SCM level. We also computed the euphotic layer depth (Z_{eu}) as the
 271 depth where the PAR is reduced to 1% of its surface value (Gordon and McCluney, 1975) and
 272 the penetration depth (Z_{pd}) calculated as $Z_{eu} / 4.6$. The surface layer corresponds to the layer
 273 extending from 0 to Z_{pd} .

274

275 **2.5 Definition of the SCM Layer**

276 To study specifically the dynamics of the bio-optical properties in the SCM layer, we
277 adjusted a Gaussian profile to each vertical profile of Chl a of the database that presented a
278 subsurface Chl a maximum and computed the width of this SCM. This parameterizing
279 approach proposed by Lewis et al., (1983) has been widely used to fit vertical profiles of Chl a
280 (e.g. Morel and Berthon, 1989; Uitz et al., 2006) such as:

$$281 \quad c(z) = c_{\max} e^{-\left(\frac{z-z_{\max}}{\Delta z}\right)^2} \quad (5)$$

282 where $c(z)$ is the Chl a concentration at depth z , c_{\max} is the Chl a concentration at the depth of
283 the SCM (z_{\max}), and Δz , the unknown, is the width of the SCM. In order to retrieve Δz , the
284 unknown parameter, we performed an optimization of equation (5) with a maximum width set
285 at 50 m so only the profiles with a relatively pronounced SCM are kept. Finally, in this study,
286 the different biogeochemical variables are averaged in this SCM layer (cf. Figures 3, 4, 6 and
287 11).

288 **2.6 Statistical method of classification of the vertical profiles providing the** 289 **identification of the SCM**

290 A statistical method based on the Singular Value Decomposition (SVD) algorithm
291 (Golub and Van Loan, 1996) was used to identify the different types of SCMs in the
292 Mediterranean Sea. The approach allowed to tackle the large amount of data provided by the
293 BGC-Argo floats and to simultaneously classify the Chl a and b_{bp} vertical profiles of the
294 database. Based on the shape of the Chl a or b_{bp} vertical profile, the method did not require an
295 *a priori* knowledge on the considered profile such as in previous studies (e.g. Uitz et al.,
296 2006; Mignot et al., 2011; Lavigne et al., 2015). The present method involved three major
297 steps summarized as follows (see Supplementary Material 2 for more details):

298 (1) Each vertical profile of $Chla$ and b_{bp} were normalized in depth and magnitude. The depths
299 were normalized by the euphotic depth (Z_{eu}) and the $Chla$ and b_{bp} values were normalized to
300 the maximum value of each profile (*i.e.* $Chla_{max}$ and b_{bpmax} , respectively). Ultimately, the
301 $Chla$ and b_{bp} values of a profile were joined by one end, to obtain a dimensionless, twice as
302 long, “metaprofile” that was subsequently classified on the basis of its shape.

303 (2) A Principal Component Analysis (PCA) was performed using the Singular Value
304 Decomposition algorithm (Pearson, 1901). The singular values were ordered in decreasing
305 order and only the first N values were kept. N was chosen so that the corresponding singular
306 vectors capture 95% of variance of the dataset and the resulting vertical profiles of $Chla$ and
307 b_{bp} were ecologically meaningful (see Supplement 2 provided as electronic supplementary
308 material).

309 (3) Each singular vector defined a profile shape. A dimensionless metaprofile can be
310 represented as a linear combination of those shapes, each multiplied by a coefficient. To
311 classify each metaprofile in a category of shape, we used a numerical optimization algorithm
312 on the whole set of coefficients to maximize the value of one coefficient while minimizing the
313 $N-1$ others, for each metaprofile. The coefficient that was maximal for each metaprofile
314 defined its class of shape. More details on the method are provided as electronic
315 supplementary material.

316 For each of the five regions of the Mediterranean considered, we finally obtained the
317 dominant shapes of vertical $Chla$ and b_{bp} profiles, which are representative of the different
318 situations encountered along an annual cycle. This approach allowed to establish a typology
319 of SCMs in the BGC-Argo database and to report their frequency of occurrence in each
320 region.

321 **3 RESULTS & DISCUSSION**

322 **3.1 Regional and seasonal variability of the SCM**

323 Using a climatological approach, we first examined the characteristics of the SCMs
324 such as their depth, thickness and amplitude in order to better apprehend their vertical
325 dynamics in the water column along the Mediterranean west-to-east gradient. Then, the
326 seasonal variations of the biogeochemical properties (Chl a and b_{bp}) at the SCM level were
327 studied in relation to environmental conditions. This ultimately led us to identify and
328 describe the main types of SCMs in the five considered regions of the Mediterranean Sea.

329 **3.1.1 Variability of the SCM along the west-to-east gradient**

330 The well-known west-to-east trophic gradient of the Mediterranean was observed in
331 the present dataset, with a decrease in the surface Chl a from the NW region (median value of
332 0.15 mg m $^{-3}$) to the LEV region (median value of 0.04 mg m $^{-3}$; Figure 3a). A decrease in the
333 amplitude of the SCM paralleled the surface gradient, with decreasing mean Chl a and b_{bp}
334 values in the SCM from the NW to the LEV (0.45 to 0.24 mg m $^{-3}$ and 0.00088 to 0.00050 m $^{-1}$
335 for Chl a and b_{bp} , respectively) (Figures 3b-c). In the Eastern Basin (*i.e.* ION and LEV), only
336 27% of the Chl a values were distributed above the median value calculated for the entire
337 Mediterranean Basin (0.28 mg m $^{-3}$) whereas 66% of the Chl a values exceeded it in the
338 Western Basin (*i.e.* NW, SW, and TYR; Figure 4). Similarly, in the Eastern Basin, only ~30%
339 of the b_{bp} values exceeded the median value calculated for the entire Mediterranean Sea in the
340 SCM (0.00058 m $^{-1}$) (*i.e.* 32% and 29% for the ION and LEV, respectively; Figures 4d-e)
341 whereas in the Western Basin, ~75% of the b_{bp} values were distributed above the global
342 median value (*i.e.* 81%, 80% and 71% for the NW, SW and TYR, respectively, Figures 4a-c).

343 In parallel, from the NW to the LEV regions, a deepening of the SCM (median values
344 of 58 and 95 m, respectively; Figure 3d) and an increase in its thickness (median values of 43
345 and 72 m, respectively; Figure 3e) was observed. A statistical Wilcoxon test revealed non-
346 identical distributions of the considered variables (SCM amplitude, depth and thickness)
347 among the different Mediterranean regions (significance level $p < 0.001$). Our results suggest
348 that the well-known west-to-east trophic gradient of the Mediterranean occurs not only at the
349 surface but also at depth. As suggested by previous studies (Mignot et al., 2014; Lavigne et
350 al., 2015), we confirm that the thickness and depth of the SCM are inversely related to its
351 amplitude. The eastward weakening, deepening and increase in the thickness of the SCM is
352 gradual across the Mediterranean Sea.

353 **3.1.2 Seasonal variations of $Chl a$ and b_{bp}**

354 The seasonal cycle of the $Chl a$ in the SCM was more pronounced in the Western
355 Basin than in the Eastern Basin. This was especially true for the NW (Figure 4a) with median
356 values of $Chl a$ reaching $\sim 0.8 \text{ mg m}^{-3}$ in June-July and $\sim 0.3 \text{ mg m}^{-3}$ in January-February.
357 Similarly, the seasonal cycle of b_{bp} in the SCM was more pronounced in the Western part of
358 the Mediterranean Sea than in the Eastern Basin. Depending on the region and period of the
359 year, the $Chl a$ and b_{bp} values showed synchronous or decoupled seasonal cycles. In the
360 Western Basin, the b_{bp} and $Chl a$ seasonal cycles were coupled. The NW and TYR regions of
361 the Western Basin showed a seasonal cycle characterized by two $Chl a$ peaks at the SCM in
362 March-April and June-July (the SW region presents a single maximum from April to July)
363 and a simultaneous increase in b_{bp} recorded in April-June (Figures 4a-c). On the opposite, the
364 ION and the LEV presented a unique maximum of $Chl a$ in June that is delayed compared to
365 the b_{bp} seasonal maximum occurring in February-April (Figures 4d-e).

366 The **Chla** is the most commonly used, yet imperfect, indicator of the phytoplankton
367 biomass (Cleveland et al., 1989; Geider, 1993). Variations in Chla may reflect changes in
368 either phytoplankton carbon (Furuya, 1990; Hodges and Rudnick, 2004; Beckmann and
369 Hense, 2007) or in intracellular content as a result of physiological processes occurring in
370 phytoplankton cells, photoacclimation in particular (Geider et al., 1997; Fennel and Boss,
371 2003). The particulate backscattering coefficient is considered as a proxy of the abundance of
372 particles (Morel and Ahn, 1991; Stramski and Kiefer, 1991; Loisel and Morel, 1998; Stramski
373 et al., 2004) and of the stock of Particulate Organic Carbon (POC) in the open ocean waters
374 (Stramski et al., 1999; Balch et al., 2001; Cetinić et al., 2012; Dall’Olmo and Mork, 2014). In
375 contrast with Chla, it provides information on the whole pool of particles, not specifically on
376 phototrophic organisms. The backscattering coefficient also depends on several parameters
377 such as the size distribution, nature, shape, structure and refractive index of the particles
378 (Morel and Bricaud, 1986; Babin and Morel, 2003; Huot et al., 2007b; Whitmire et al., 2010).

379 The vertical and seasonal coupling of Chla and b_{bp} has been shown to reflect an actual
380 increase in carbon biomass whereas a decoupling could result from photoacclimation or from
381 a change in the nature or size distribution of the particle assemblage (Flory et al., 2004;
382 Behrenfeld et al., 2005; Siegel et al., 2005). The results presented above indicate that the
383 Western Basin presents higher values of Chla and b_{bp} in the SCM compared to the Eastern
384 Basin and displays a coupling of the properties all year long (Figure 4). Hence, we suggest
385 that in the NW, SW and TYR regions, the SCM sustains larger phytoplankton carbon biomass
386 than in the ION and LEV regions. Furthermore, in this Eastern part of the Mediterranean Sea,
387 the SCM results, at first order, from physiological acclimation to low light and/or from a
388 modification of the nature of the particle assemblage. In the next section, we will analyse the
389 environmental conditions occurring at the SCM level and attempt to determine the factors
390 underpinning the seasonal occurrence of SCMs in the different regions.

391 3.1.3 Environmental factors controlling the SCM

392 From a bottom-up perspective, it is the balance between light and nutrient limitations
393 that influences the establishment of phytoplankton communities at depth (Kiefer et al., 1976;
394 Cullen, 1982; Klausmeier and Litchman, 2001; Ryabov, 2012; Latasa et al., 2016). To explore
395 the light-nutrient regime within the SCM layer, a monthly climatology of the isolume and
396 nitracline in the different considered regions was represented along with the depth of the
397 Subsurface Chl a and b_{bp} Maxima (*i.e.* SCM and $Sb_{bp}M$, respectively). The MLD was also
398 superimposed in order to illustrate physical forcings (Figure 5).

399 In the Western Basin, the isolume $0.3 \text{ mol quanta m}^{-2} \text{ d}^{-1}$, the nitracline $1 \text{ } \mu\text{mol}$, the
400 $Sb_{bp}M$ and the SCM were all located at a similar depth during the oligotrophic period
401 (maximum depth difference $< 20 \text{ m}$; Figures 5a-c). In accordance with previous findings (*e.g.*
402 Pasqueron de Fommervault et al., 2015a), our results suggest that in the NW region of the
403 Mediterranean Sea, the winter deepest climatological mixed layer depth reached the
404 nutricline, thus likely inducing nutrient input to the surface layer. In the TYR region, the
405 MLD was always shallower than the nutricline during the winter season but the difference
406 between the MLD and the nutricline remained very small all year long. Hence, in the Western
407 Basin of the Mediterranean Sea both light and nutrient resources seem to be available and
408 probably support an actual increase in phytoplankton biomass (Figures 5 and 6a-b). In the
409 Northwestern part of the Mediterranean Sea, the MLD was deeper than the nutricline $\sim 20\%$ of
410 the time during an annual cycle (Figure 6e) essentially during the winter season (Figure 5 a-
411 c). The shallowest (median of 61 m ; Figure 6c) and the steepest (slope of $90 \text{ } \mu\text{mol m}^{-4}$; Figure
412 6d) nitraclines were also recorded in this region, thus confirming an important upward
413 diffusive flux of nitrates available to sustain phytoplankton biomass and eventually allowed
414 the occurrence of a Subsurface Biomass Maximum.

415 In contrast, in the ION and LEV regions, the isolume $0.3 \text{ mol quanta m}^{-2} \text{ d}^{-1}$, nitracline 1
416 μmol , SCM and $S_{b_{bp}M}$ were not collocated in the water column (Figures 5d-e). The
417 difference between the depths of the SCM and nitracline was $\sim 50 \text{ m}$ during the stratified
418 period (Figures 5d-e and 6a) and the $S_{b_{bp}M}$ was shallower than the SCM (by $\sim 40 \text{ m}$),
419 suggesting that the standing stock of carbon is maintained at a higher concentration above the
420 depth of the SCM. In the Eastern Basin (Ionian and Levantine Sea), the MLD almost never
421 reached the nutricline even during the winter period as it was deeper than the nutricline only
422 $<3\%$ of the time during an annual cycle (Figure 6e). The nutricline was deeper ($\sim 120 \text{ m}$ in
423 Eastern Basin *versus* $\sim 70 \text{ m}$ in Western Basin; Figure 6c) and the nutrient gradient was also
424 less sharp (nitracline slope of $\sim 40 \mu\text{mol m}^{-4}$ in Eastern Basin versus $\sim 90 \mu\text{mol m}^{-4}$ in Western
425 Basin; Figure 6d) than in the Western part of the Mediterranean Sea, suggesting a weak
426 upward diffusive flux of nitrates that corroborates previous results (Tanhua et al., 2013;
427 Pasqueron de Fommervault et al., 2015b). The inverse relationship between the nitracline
428 steepness and the thickness of the SCM is also confirmed (Gong et al., 2017). The PAR at the
429 SCM level was significantly lower in this Eastern part than in the Western part of the
430 Mediterranean Sea (Wilcoxon test at a significance level of $p < 0.001$; Figure 6b). The
431 development of the SCM in this system is, thus, likely to be limited by both the availability of
432 light and nutrients. The SCM still settles at a depth where light is available at a sufficient level
433 to sustain photosynthesis, but never reaches the nitracline.

434 **3.1.4 Coupling and decoupling of b_{bp} and $Chl a$ in the SCM**

435 We have seen that the SCM of the Western Basin benefits from both light and nutrient
436 resources. In these conditions, the observed simultaneous increase in $Chl a$ and b_{bp} at the SCM
437 most likely represents an actual development of phytoplankton biomass, as indicated by the
438 concordance between the depths of the SCM and the $S_{b_{bp}M}$ (Figure 5). On the opposite, in the
439 Eastern part of the Mediterranean Sea, the maxima of $Chl a$ and b_{bp} are not co-located. This

440 result suggests that environmental conditions, typically the light conditions, might inhibit the
441 increase in phytoplankton biomass.

442 In the Eastern Basin of the Mediterranean Sea, the microorganisms are, most probably,
443 acclimated or even adapted to the environmental conditions. While photoacclimation is
444 defined as a short-term acclimation of a photosynthetic organism to changing irradiance,
445 photoadaptation refers to the long-term evolutionary adaptation of photosynthetic organisms
446 to ambient light conditions, through genetic selection. SCM species are known to use
447 different strategies such as photoacclimation to low light (*i.e.* increase in the intracellular
448 pigment content), mixotrophy or small-scale directed movements towards light (Falkowski
449 and Laroche, 1991; Geider et al., 1997; Clegg et al., 2012). Phytoplankton species are also
450 likely to have different carbon-to-chlorophyll ratio (Falkowski et al., 1985; Geider, 1987;
451 Cloern et al., 1995; Sathyendranath et al., 2009) and b_{bp} properties (Vaillancourt et al., 2004;
452 Whitmire et al., 2010), and a vertical shift toward species photoadapted to the particular
453 environmental conditions prevailing in the SCM layer is a well-known phenomenon (*e.g.*
454 Pollehne et al., 1993; Latasa et al., 2016). For example, two ecotypes of *Prochlorococcus*,
455 characterized by different accessory pigment contents are known to be adapted to either low-
456 light or high-light conditions and to occupy different niches in the water column (Moore and
457 Chisholm, 1999; Bouman et al., 2006; Garczarek et al., 2007). In particular, the low-light
458 ecotype, characterized by increased intracellular pigmentation, has been frequently observed
459 at the SCM level in the Mediterranean, especially in the Eastern part (Brunet et al., 2006;
460 Siokou-Frangou et al., 2010). A west-to-east modification in the composition of
461 phytoplankton communities in the SCM toward a dominance of picophytoplankton species
462 adapted to recurring light limitation, has been observed (Christaki et al., 2001; Siokou-
463 Frangou et al., 2010; Crombet et al., 2011). A vertical decoupling between b_{bp} and Chl a could

464 thus illustrate either a photoacclimation of phytoplankton cells or the occurrence of specific
465 phytoplankton communities adapted to the conditions prevailing in the SCM layer.

466 Although photoacclimation seems to be a widespread hypothesis in numerous studies to
467 explain the vertical decoupling of $Chla$ and b_{bp} (e.g. Brunet et al., 2006; Cullen, 1982; Mignot
468 et al., 2014), it should yet be reminded that this decoupling could also result from a change in
469 the nature or size distribution of the entire particle pool. Small particles are, for example,
470 known to backscatter light more efficiently than large particles (Morel and Bricaud, 1986;
471 Stramski et al., 2004). A higher proportion of nonalgal particles in the Eastern compared to
472 the Western Basin could thus explain the decoupling between b_{bp} and $Chla$. The nonalgal
473 particles compartment is defined as the background of submicronic living biological cells (*i.e.*
474 viruses or bacteria) and non-living particles (*i.e.* detritus or inorganic particles) and is
475 typically known to represent a significant part of the particulate assemblage in oligotrophic
476 ecosystems (Morel and Ahn, 1991; Claustre et al., 1999; Stramski et al., 2001).

477 Finally, photoacclimation processes as well as vertical gradients in phytoplankton
478 species or in the non-phytoplankton particles, also contributing to b_{bp} , could explain the
479 vertical decoupling of b_{bp} and $Chla$ we observed in the Eastern Basin. The different types of
480 $Chla$ and b_{bp} vertical profiles depends on both the nature of the particles present in the water
481 column, the physiology of phytoplanktonic cells and their related bio-optical properties, but
482 yet our dataset did not allow us to conclude on the dominance of one process compared to the
483 other.

484 **3.2 Classification of the $Chla$ and b_{bp} vertical profiles**

485 In the previous section, we identified the major environmental factors leading to the
486 occurrence of two main types of SCMs in the five considered regions of the Mediterranean
487 Sea. While a concomitant maximum of $Chla$ and b_{bp} suggested a carbon biomass maximum, a

488 decoupling between the vertical distributions of these two properties may reflect
489 photoacclimation, a modification of the algal community composition, or a change in the
490 nature and/or size of the particle assemblage. The seasonal and regional variability in this
491 global picture of the SCM was explored using a statistical approach applied to the BGC-Argo
492 dataset. Our aim was here to classify the *Chla* and b_{bp} profiles based on their shape. This
493 led us to propose a typology of the different types of SCMs seasonally encountered in the
494 five regions of the Mediterranean Sea. It also permitted to assess the frequency of these
495 different types of SCMs over the seasonal cycle and compare their characteristics among the
496 various regions of the Mediterranean Sea.

497 **3.2.1 The NW: a region with a specific trophic regime**

498 In the NW, the vertical distributions of *Chla* and b_{bp} presented four different shapes
499 over the annual cycle (Figures 7a-b). The *mixed* shape was characterized by a homogeneous
500 distribution of *Chla* and b_{bp} (as suggested by the deep mean MLD associated with this type of
501 profile; Figures 7a-b) and showed occurrence exceeding 60% from December to March
502 (Figure 8a). The *bloom* shape exhibited high *Chla* and b_{bp} values at surface with maximum
503 occurrence > 55% in April. The coexistence of the *mixed* and the *bloom* shapes during winter
504 and spring could result from intermittent mixing that alters the vertical distribution of *Chla*
505 and b_{bp} (e.g. Chiswell, 2011; Lacour et al., 2017). The SBM_{aZeu} and the SBM_{bZeu} (SBM
506 occurring above and below the euphotic depth, respectively) constituted two different cases of
507 subsurface maximum. In both cases, *Chla* and b_{bp} covaried (Figures 7a-b), the maxima of
508 *Chla* and b_{bp} were observed at nearly the same depth suggesting an increase in carbon
509 biomass in subsurface.

510 The SBM_{aZeu} was often observed in late spring and late summer whereas the SBM_{bZeu}
511 occurred more frequently (> 50%) in the middle of the oligotrophic period. This results

512 suggests a deepening of the SCM along the oligotrophic season and corroborates the “light-
513 driven hypothesis” previously formulated by Letelier et al. (2004) and Mignot et al. (2014).
514 These authors observed that the seasonal variation of the depth of the SCM depicts the same
515 displacement as the isolumes and consequently suggested that the SCM depth displacement is
516 light-driven. In the NW region, the high surface Chla of the *bloom* shape (Figure 7a) probably
517 results in increased light attenuation in the water column from fall to spring. Consequently,
518 the SCM established shallower in spring than in summer (Figure 5a) and the SBM_{aZeu} shape
519 occurred relatively frequently in spring (Figure 8a). Then, from spring to summer, the Chla
520 decrease in the surface layer of the water column resulted in decreased light attenuation and
521 subsequent deepening of the SCM (Figure 5a), which thus formed a subsurface maximum of
522 Chla and b_{bp} below the euphotic layer (SBM_{bZeu} , Figure 8a). Therefore, our results are
523 consistent with previous studies (e.g. Gutiérrez-Rodríguez et al., 2010; Mayot et al., 2017b)
524 that highlighted the special status of the Northwestern region, the only region to exhibit the
525 *bloom* shape and predominantly SBMs during the oligotrophic season (Figures 9a-b).

526 3.2.2 The SW and the TYR: regions of transition

527 In the Southwestern region as well as in the Tyrrhenian Sea, three shapes characterized
528 the seasonal variability of the vertical distribution of Chla and b_{bp} (Figures 7c-d and e-f). A
529 *mixed* shape, similar to that observed in the NW (Figures 9c-d), a *SBM* shape (Figures 9e-f),
530 and a *SCM* shape (decoupling between the maximum of Chla and b_{bp} at depth) were
531 successively encountered over the seasonal cycle, with weak differences in their frequency of
532 occurrence among the two regions. The *SCM* shape established shallower in the water column
533 than the *SBM* shape (Figures 7c-f). It was encountered mainly in winter and fall (~50% of
534 occurrence), alternating with the *mixed* shape (Figures 8b-c). Thus, this shape probably
535 illustrates the erosion of the SCM by the winter mixing as previously suggested, for example,
536 in Lavigne et al. (2015). The *SBM* shape occurred mainly during spring and summer (>75%)

537 when both light and nutrients were available for phytoplankton growth (Figures 5b-c). The
538 *SBM* shapes of the SW and the TYR were comparable to the *SBM_{bZeu}* shape of the NW
539 occurring at almost the same depth ($\sim Z_{eu}$). The *SCM* shapes of the SW and TYR were
540 analogous to the *SCM_{aZeu}* shape of the ION and LEV (Figures 9e-h). Hence, our results
541 suggest that the SW and TYR regions are transition regimes that present types of SCMs that
542 can be found in both the Western and Eastern Basins.

543 **3.2.3 The ION and the LEV: oligotrophic end-members**

544 In the Ionian Sea, three different shapes were retrieved along the seasonal cycle, *i.e.* the
545 *mixed*, the *SCM_{aZeu}* and the *SCM_{bZeu}* shapes (Figures 7g-h). In this region, the Chl_a maximum
546 was always decorrelated from the b_{bp} maximum that revealed higher values at surface than at
547 depth. In the Levantine Sea, only two distinct shapes were encountered, *i.e.* the *SCM_{aZeu}* and
548 the *SCM_{bZeu}* shapes and associated with shallow MLDs (Figures 7i-j). The subsurface
549 maximum of Chl_a was never associated with a subsurface maximum of b_{bp} . Such SCMs
550 constituted a permanent pattern with *SCM_{bZeu}* and *SCM_{aZeu}* reaching occurrences of 100% in
551 June-July and $> 75\%$ in December-March, respectively (Figures 8d-e). The *SCM_{bZeu}* shape
552 was a particularity of the Eastern Basin. This shape was very similar in the ION and LEV, but
553 very different from the shapes observed in the other regions (Figures 9g-h). This *SCM_{bZeu}*
554 settled below the Z_{eu} that, in such oligotrophic systems, occurs relatively deep in the water
555 column (~ 95 m; Figure 3d). This type of SCM was also very thick (~ 70 m) (Figure 3e) and
556 associated with low values of the nitracline slope (Figure 6d).

557 **3.3 A case study of the Gulf of Lions and Levantine Sea**

558 Both the climatological and statistical approaches proposed in this study allowed us to
559 characterize the SCM dynamics in five regions of the Mediterranean Sea at large spatial
560 (interregional) and temporal (seasonal) scales. In the present section, we focused on the data

561 provided by two BGC-Argo floats that recorded simultaneously bio-optical properties, PAR
562 and nitrate concentration in two distinct regions, representing the two extremes of the
563 Mediterranean trophic gradient. This helped to gain understanding of the dynamics of the
564 SCM at a weekly and regional scale and should give insights in the mechanisms underlying
565 the occurrence of SCMs in these end-member regimes.

566 **3.3.1 Overview of the two contrasted systems**

567 The float WMO 6901512 (fGL) was been deployed in the Gulf of Lions the 11th of
568 April 2013 and recorded data until the 4th of May, 2014 (Figure 10a). The float WMO
569 6901528 (fLS) collected data in the Levantine Sea from May 18, 2013 to May 23, 2015
570 (Figure 10c). The two regions presented very different seasonal Chl*a* distribution. The Gulf of
571 Lions is a typical “temperate-like” system that exhibits a winter period characterized by large
572 MLDs (Millot, 1999; Lavigne et al., 2015) (maximum MLD > 1000 m, Figure 10d). The
573 intense mixing induces a refueling of nutrients (Gačić et al., 2002; D’Ortenzio et al., 2014;
574 Severin et al., 2017), which allows the development of a spring bloom (Marty et al., 2002,
575 2008; Mayot et al., 2017a) as revealed by the high surface Chl*a* from April to May (Figure
576 10b). A subsurface maximum of Chl*a* established from the end of May to mid-November at a
577 depth similar to that of the nitracline $1 \mu\text{M}$ and isolume $0.3 \text{ mol quanta m}^{-2} \text{ d}^{-1}$, and displayed
578 maximum Chl*a* of $\sim 1 \text{ mg m}^{-3}$ in July (Figure 10b).

579 The Levantine Sea behaves, on the opposite, as a “tropical-like” system. Winter mixing
580 was weak (maximum MLD of 125 m; Figure 10d) but still able to erode the SCM as
581 suggested by the small increase in surface Chl*a* from November to February (Figure 10b).
582 The seasonal MLD deepening almost never reached the nitracline, thus limiting the nitrate
583 supply to the upper layer of the water column (Dugdale and Wilkerson, 1988; Lavigne et al.,
584 2013; Pasqueron de Fommervault et al., 2015a), hence leading to relatively low surface

585 primary production in this area (Krom et al., 1991; Psarra et al., 2000; Bricaud et al., 2002;
586 Siokou-Frangou et al., 2010). The SCM is a permanent feature in this region, settling below
587 the isolume $0.3 \text{ mol quanta m}^{-2} \text{ d}^{-1}$ and far above the nitracline (Figure 10d).

588 **3.3.2 Factors limiting the SCM**

589 For exploring the limiting factors at the level of the SCM, we used a nutrient-vs-light
590 resource-limitation diagram. This approach employed in biogeochemical modelling (Cloern,
591 1999; Li and Hansell, 2016) exploits simultaneously PAR and $[\text{NO}_3^-]$ data in order to
592 understand which environmental factor limits phytoplankton growth (Figure 11).

593 In the Gulf of Lions, two different types of situations occurred: (1) very low light compared to
594 the maximum surface PAR ($\text{PAR}_{\text{norm}} < 0.025$) coupled with $\text{NO}_3^-_{\text{norm}}$ comprised between 0
595 and 1, indicative of light limitation; and (2) low light compared to the maximum surface PAR
596 (PAR_{norm} within the range 0.025-0.15) associated with $\text{NO}_3^-_{\text{norm}} < 0.15$, indicative of nitrate
597 limitation, probably resulting from uptake by phytoplankton (Figure 11a). On the contrary, in
598 the Eastern part of the Mediterranean Sea, the SCM was always associated with very low light
599 conditions compared to the maximum surface PAR ($\text{PAR}_{\text{norm}} < 0.025$) and variable $\text{NO}_3^-_{\text{norm}}$
600 values comprised between 0.1 and 1 (Figure 11b). This suggests that, even when the nitrate
601 concentration is sufficient to sustain primary production at the SCM level, another factor
602 limits phytoplankton growth. Phytoplankton growth at the SCM is probably limited by light
603 or co-limited by both light and nutrients. Phosphate is also an important limiting factor for
604 phytoplankton growth in the entire Mediterranean Sea (Marty et al., 2002; Pujo-Pay et al.,
605 2011), the Eastern Basin in particular (Krom et al., 1991, 2010). Hence, in a non-nitrate
606 limited SCM of the Levantine (Figure 11b), phytoplankton may still be limited by either or
607 both low phosphate concentrations and low light levels. Since autonomous measurements of

608 phosphate concentrations are not possible yet, our chemical data are restricted to nitrate so we
609 cannot conclude on the role of phosphate in the settlement of the SCM.

610 The coupling between $Chl a$ and b_{bp} was studied using the $Chl a$ -to- b_{bp} ratio. In both the
611 Western and Eastern Basins, SCMs with prevailing very low light conditions were
612 accompanied by high values of the $Chl a$ -to- b_{bp} ratio ($> 300 \text{ mg m}^{-2}$). In contrast, in the SCM
613 of the Western Basin associated with low values of $NO_3^-_{norm}$, the $Chl a$ -to- b_{bp} ratio showed
614 values $< 300 \text{ mg m}^{-2}$. This ratio is a proxy of the $Chl a$ -to-POC ratio (Behrenfeld et al., 2015;
615 Álvarez et al., 2016; Westberry et al., 2016) and constitutes an optical index of
616 photoacclimation (Behrenfeld et al., 2005; Siegel et al., 2005) or of the phytoplankton
617 communities (Cetinić et al., 2012, 2015). Hence, in both the Western and Eastern Basins, the
618 high values of the $Chl a$ -to- b_{bp} ratio occurring in the SCM associated with very low light
619 conditions could be attributed to either photoacclimation of phytoplankton cells to low light
620 intensity. In contrast, in the SCM of the Western Basin where low values of $NO_3^-_{norm}$ were
621 reported, the low $Chl a$ -to- b_{bp} ratio values could either indicate a higher proportion of detrital
622 particles or an increase in biomass sustained by a specific phytoplankton assemblage
623 dominated by communities of nano- or pico-sized cells, including very small diatoms (*e.g.*
624 Leblanc et al., 2018).

625 **4 CONCLUSIONS**

626 The present study is, to our knowledge, the first examining the spatial and temporal
627 variability of Subsurface Chlorophyll a Maxima (SCMs) in the Mediterranean Sea using
628 BioGeochemical-Argo profiling floats equipped with both light (PAR) and nitrate ($[NO_3^-]$)
629 sensors. Our study aims to improve the understanding of the characteristics and dynamics of
630 phytoplankton biomass in the subsurface layer of the Mediterranean Sea. We identified two
631 major mechanisms controlling the occurrence of SCMs, *i.e.* (1) SCMs arising from an actual

632 increase in carbon biomass most probably reflecting an increase in phytoplankton biomass
633 benefiting from both light and nutrient resources (SBMs) with a potentially non negligible
634 contribution of non-phytoplankton particles at depth; and (2) SCMs that stem from an
635 increase in intracellular **Chl a** as a result of photoacclimation to low light levels. In the
636 temperate-like system of the Western Mediterranean Sea, SBMs are recurrent whereas in the
637 “subtropical-like” system of the Eastern Mediterranean Sea, SCMs are, at a first order,
638 representative of photoacclimation process. Using a statistical classification of vertical
639 profiles of Chl a and b_{bp} collected over the entire Mediterranean, we have evidenced different
640 intermediate SCM situations that can be summarized as follows (Figure 12):

641 1) The SBM $_{aZeu}$ is a Subsurface Biomass Maximum that settles above the euphotic zone
642 in the Northwestern Mediterranean Sea (NW). It is the thinnest (~40m) and shallowest (~60
643 m) biomass maximum. It is also the most intense, probably because it benefits from adequate
644 light and nutrient resources, with the deep mixed layer occurring in this region during the
645 winter period probably inducing a seasonal renewal of the nutrients in the surface layer.

646 2) The SBM $_{bZeu}$ establishes below the euphotic zone in the NW. As well as the SBMs of
647 the Southwestern Mediterranean Sea (SW) and Tyrrhenian Sea (TYR), less intense than the
648 SBM $_{aZeu}$ probably because nutrients conditions are less favourable than in the NW region as
649 the winter MLD is close to, but never reaches the nutricline.

650 3) The SCM of the SW and TYR as well as the SCM $_{aZeu}$ (*i.e.* settling above the euphotic
651 depth) of the Ionian (ION) and Levantine (LEV) Seas are not biomass subsurface maxima,
652 but reflect Chl a maxima resulting from photoacclimation. Moving from the SW to LEV
653 region, the amplitude of the SCM decreases while its thickness increases.

654 4) The SCM $_{bZeu}$ of the ION and LEV settle below the euphotic depth and are deeper
655 (~95 m) than all the other subsurface maxima. They are most probably the consequence of a
656 decoupling of the MLD and the nutricline and represent the oligotrophic end-member type of

657 subsurface maxima in the Mediterranean Sea. In these types of SCMs, phytoplankton
658 communities most probably establish deep in the water column, in order to reach the nutrient
659 resources. These communities are likely photoacclimated, and also possibly photoadapted, to
660 the low light conditions encountered at such depths. The phytoplankton assemblage is likely
661 composed of picophytoplankton (Casotti et al., 2003; Siokou-Frangou et al., 2010), including
662 the low-light adapted *Prochlorococcus* ecotype (Brunet et al., 2006; Garczarek et al., 2007).

663 In permanently stratified oligotrophic ecosystems, the SCM phytoplankton species may
664 settle especially deep and adapt to the prevailing low-light levels in order to benefit from
665 more nutrients. On the contrary, when nitrates are not a limiting factor at the SCM level (e.g.
666 in the northwestern region after the bloom period), the SCM is only controlled by the amount
667 of light available at depth. In either case, light is a crucial forcing parameter that controls the
668 depth of the SCM. Consistently with previous studies conducted in other open ocean regions
669 (Longhurst and Glen Harrison, 1989; Furuya, 1990; Severin et al., 2017), the present work
670 suggests that shallower SCMs tend to display larger phytoplankton biomass than deeper
671 SCMs. In our study, these biomass maxima are characterized by a coupling of Chl a and b_{bp}
672 that suggests an increase in carbon biomass. Finally, the present results indicate that SBMs
673 represent a frequent feature in the Mediterranean Sea, which contrasts with the idea that
674 SCMs in oligotrophic regions typically result from photoacclimation of phytoplankton cells.
675 Thus, we suggest that the contribution of SCMs to primary production, which may be
676 substantial although ignored by current satellite-based estimates, should be further
677 investigated.

678 **ACKNOWLEDGEMENTS**

679 This paper represents a contribution to the following research projects: remOcean
680 (funded by the European Research Council, grant 246777), NAOS (funded by the Agence

681 Nationale de la Recherche in the frame of the French “Equipped d’avenir” program, grant
682 ANR J11R107-F), the SOCLIM (Southern Ocean and climate) project supported by the
683 French research program LEFE- CYBER of INSU-CNRS, the Climate Initiative of the
684 foundation BNP Paribas and the French polar institute (IPEV), AtlantOS (funded by the
685 European Union’s Horizon 2020 Research and Innovation program, grant 2014– 633211), E-
686 AIMS (funded by the European Commission’s FP7 project, grant 312642), U.K. Bio-Argo
687 (funded by the British Natural Environment Research Council—NERC, grant NE/
688 L012855/1), REOPTIMIZE (funded by the European Union’s Horizon 2020 Research and
689 Innovation program, Marie Skłodowska-Curie grant 706781), Argo-Italy (funded by the
690 Italian Ministry of Education, University and Research - MIUR), and the French Bio-Argo
691 program (BGC-Argo France; funded by CNES-TOSCA, LEFE Cyber, and GMMC). We
692 thank the PIs of several BGC-Argo floats missions and projects: Giorgio Dall’Olmo
693 (Plymouth Marine Laboratory, United Kingdom; E-AIMS and U.K. Bio- Argo); Kjell-Arne
694 Mork (Institute of Marine Research, Norway; E-AIMS); Violeta Slabakova (Bulgarian
695 Academy of Sciences, Bulgaria; E-AIMS); Emil Stanev (University of Oldenburg, Germany;
696 E-AIMS); Claire Lo Monaco (Laboratoire d’Océanographie et du Climat: Expérimentations et
697 Approches Numériques); Pierre-Marie Poulain (National Institute of Oceanography and
698 Experimental Geophysics, Italy; Argo- Italy); Sabrina Speich (Laboratoire de Météorologie
699 Dynamique, France; LEFE- GMMC); Virginie Thierry (Ifremer, France; LEFE-GMMC);
700 Pascal Conan (Observatoire Océanologique de Banyuls sur mer, France; LEFE-GMMC);
701 Laurent Coppola (Laboratoire d’Océanographie de Villefranche, France; LEFE-GMMC);
702 Anne Petrenko (Mediterranean Institute of Oceanography, France; LEFE-GMMC); and Jean-
703 Baptiste Sallée (Laboratoire d’Océanographie et du Climat, France; LEFE-GMMC). Louis
704 Prieur and Jean-Olivier Irisson (Laboratoire d’Océanographie de Villefranche, France) are
705 acknowledged for useful comments and fruitful discussion. We also thank the International

706 Argo Program and the CORIOLIS project that contribute to make the data freely and publicly
707 available.

708 REFERENCES

709 Álvarez, E., Morán, X. A. G., López-Urrutia, Á. and Nogueira, E.: Size-dependent photoacclimation of the
710 phytoplankton community in temperate shelf waters (southern Bay of Biscay), *Marine Ecology Progress Series*, 543, 73–87,
711 doi:10.3354/meps11580, 2016.

712 Anderson, G. C.: Subsurface Chlorophyll Maximum in the Northeast Pacific Ocean, *Limnology and Oceanography*,
713 14(3), 386–391, 1969.

714 Antoine, D., Morel, A. and André, J.-M.: Algal pigment distribution and primary production in the eastern
715 Mediterranean as derived from coastal zone color scanner observations, *Journal of Geophysical Research*, 100, 16193–
716 16209, 1995.

717 Arai, R., Nishiyama, N., Nakatani, N. and Okuno, T.: Measurement Method of Nutrient using Principal Component
718 Regression, in *OCEANS 2008-MTS/IEEE Kobe Techno-Ocean*, IEEE., pp. 1–6., 2008.

719 Ardyna, M., Babin, M., Gosselin, M., Devred, E., Bélanger, S., Matsuoka, A. and Tremblay, J. E.: Parameterization
720 of vertical chlorophyll a in the Arctic Ocean: Impact of the subsurface chlorophyll maximum on regional, seasonal, and
721 annual primary production estimates, *Biogeosciences*, 10(6), 4383–4404, doi:10.5194/bg-10-4383-2013, 2013.

722 Arrigo, K. R., Matrai, P. A. and Van Dijken, G. L.: Primary productivity in the Arctic Ocean: Impacts of complex
723 optical properties and subsurface chlorophyll maxima on large-scale estimates, *Journal of Geophysical Research: Oceans*,
724 116(11), 1–15, doi:10.1029/2011JC007273, 2011.

725 Babin, M., Morel, A., Fournier-Sicre, V., Fell, F. and Stramski, D.: Light scattering properties of marine particles in
726 coastal and open ocean waters as related to the particle mass concentration, *Limnology and Oceanography*, 48(2), 843–859,
727 doi:10.4319/lo.2003.48.2.0843, 2003.

728 Balch, W. M., Drapeau, D. T., Fritz, J. J., Bowler, B. C. and Nolan, J.: Optical backscattering in the Arabian Sea—
729 continuous underway measurements of particulate inorganic and organic carbon, *Deep Sea Research Part I: Oceanographic*
730 *Research Papers*, 48(11), 2423–2452, doi:10.1016/S0967-0637(01)00025-5, 2001.

731 Barbieux, M., Uitz, J., Bricaud, A., Organelli, E., Poteau, A., Schmechtig, C., Gentili, B., Penker, C., Leymarie,
732 E., D’Ortenzio, F. and Claustre, H.: Assessing the Variability in the Relationship Between the Particulate Backscattering
733 Coefficient and the Chlorophyll *a* Concentration From a Global Biogeochemical-Argo Database, *Journal of Geophysical*

734 Research: Oceans, 123(2), 1229–1250, doi:10.1002/2017JC013030, 2017.

735 Beckmann, A. and Hense, I.: Beneath the surface: Characteristics of oceanic ecosystems under weak mixing
736 conditions - A theoretical investigation, *Progress in Oceanography*, 75(4), 771–796, doi:10.1016/j.pocean.2007.09.002, 2007.

737 Behrenfeld, M. J., Boss, E., Siegel, D. A. and Shea, D. M.: Carbon-based ocean productivity and phytoplankton
738 physiology from space, *Global Biogeochemical Cycles*, 19(GB1006), 1–14, doi:10.1029/2004GB002299, 2005.

739 Behrenfeld, M. J., O'Malley, R. T., Boss, E. S., Westberry, T. K., Graff, J. R., Halsey, K. H., Milligan, A. J., Siegel,
740 D. A. and Brown, M. B.: Revaluating ocean warming impacts on global phytoplankton, *Nature Climate Change*, 6(3), 323–
741 330, doi:10.1038/nclimate2838, 2015.

742 Bethoux, J. P., Morin, P., Madec, C. and Gentili, B.: Phosphorus and nitrogen behaviour in the Mediterranean Sea,
743 *Deep Sea Research Part A, Oceanographic Research Papers*, 39(9), 1641–1654, doi:10.1016/0198-0149(92)90053-V, 1992.

744 Bosc, E., Bricaud, A. and Antoine, D.: Seasonal and interannual variability in algal biomass and primary production
745 in the Mediterranean Sea, as derived from 4 years of SeaWiFS observations, *Global Biogeochemical Cycles*, 18(GB1005), 1–
746 17, doi:10.1029/2003GB002034, 2004.

747 Boss, E., Picheral, M., Leeuw, T., Chase, A., Karsenti, E., Gorsky, G., Taylor, L., Slade, W., Ras, J. and Claustre, H.:
748 The characteristics of particulate absorption, scattering and attenuation coefficients in the surface ocean; Contribution of the
749 Tara Oceans expedition, *Methods in Oceanography*, 7, 52–62, doi:10.1016/j.mio.2013.11.002, 2013.

750 Bouman, H., Ulloa, O., Scanlan, D. J., Zwirgmaier, K., Li, W. K. W., Platt, T., Stuart, V., Barlow, R., Leth, O.,
751 Clementson, L., Lutz, V. A., Fukasawa, M., Watanabe, S. and Sathyendranath, S.: Oceanographic Basis of the Global
752 Surface Distribution of *Prochlorococcus* Ecotypes, *Science*, 312(5775), 918–921, doi:10.1126/science.39.1002.398, 2006.

753 de Boyer Montégut, C.: Mixed layer depth over the global ocean: An examination of profile data and a profile-based
754 climatology, *Journal of Geophysical Research*, 109(C12), 1–20, doi:10.1029/2004JC002378, 2004.

755 Bricaud, A., Bosc, E. and Antoine, D.: Algal biomass and sea surface temperature in the Mediterranean Basin
756 Intercomparison of data from various satellite sensors, and implications for primary production estimates, *Remote Sensing of*
757 *Environment*, 81(2–3), 163–178, doi:10.1016/S0034-4257(01)00335-2, 2002.

758 Briggs, N., Perry, M. J., Cetinić, I., Lee, C., D'Asaro, E., Gray, A. M. and Rehm, E.: High-resolution observations of
759 aggregate flux during a sub-polar North Atlantic spring bloom, *Deep Sea Research Part I: Oceanographic Research Papers*,
760 58(10), 1031–1039, doi:10.1016/j.dsr.2011.07.007, 2011.

761 Brunet, C., Casotti, R., Vantrepotte, V., Corato, F. and Conversano, F.: Picophytoplankton diversity and
762 photoacclimation in the Strait of Sicily (Mediterranean Sea) in summer. I. Mesoscale variations, *Aquatic Microbial Ecology*,
763 44(2), 127–141, doi:10.3354/ame044127, 2006.

764 Casotti, R., Landolfi, A., Brunet, C., D'Ortenzio, F., Mangoni, O. and Ribera d'Alcalá, M.: Composition and
765 dynamics of the phytoplankton of the Ionian Sea (eastern Mediterranean), *Journal of Geophysical Research*, 108(C9), 1–19,
766 doi:10.1029/2002JC001541, 2003.

767 Cetinić, I., Perry, M. J., Briggs, N. T., Kallin, E., D'Asaro, E. A. and Lee, C. M.: Particulate organic carbon and
768 inherent optical properties during 2008 North Atlantic Bloom Experiment, *Journal of Geophysical Research*, 117(C06028),
769 1–18, doi:10.1029/2011JC007771, 2012.

770 Cetinić, I., Perry, M. J., D'Asaro, E., Briggs, N., Poulton, N., Sieracki, M. E. and Lee, C. M.: A simple optical index
771 shows spatial and temporal heterogeneity in phytoplankton community composition during the 2008 North Atlantic Bloom
772 Experiment, *Biogeosciences*, 12(7), 2179–2194, doi:10.5194/bg-12-2179-2015, 2015.

773 Chiswell, S. M.: Annual cycles and spring blooms in phytoplankton: Don't abandon Sverdrup completely, *Marine*
774 *Ecology Progress Series*, 443, 39–50, doi:10.3354/meps09453, 2011.

775 Christaki, U., Giannakourou, A., Van Wambeke, F. and Grégori, G.: Nanoflagellate predation on auto- and
776 heterotrophic picoplankton in the oligotrophic Mediterranean Sea, *Journal of Plankton Research*, 23(11), 1297–1310,
777 doi:10.1093/plankt/23.11.1297, 2001.

778 Claustre, H., Morel, A., Babin, M., Cailliau, C., Marie, D., Marty, J.-C., Tailliez, D. and Vault, D.: Variability in
779 particle attenuation and chlorophyll fluorescence in the tropical Pacific: Scales, patterns, and biogeochemical implications,
780 *Journal of Geophysical Research*, 104(C2), 3401–3422, 1999.

781 Claustre, H., Bishop, J., Boss, E., Bernard, S., Berthon, J.-F., Coatanoan, C., Johnson, K. S., Lotiker, A., Ulloa, O.,
782 Perry, M. J., D'Ortenzio, F., Hembise Fanton D'andon, O. and Uitz, J.: Bio-optical profiling floats as new observational tools
783 for biogeochemical and ecosystem studies: Potential synergies with ocean color remote sensing., in "Proceedings of the
784 OceanObs'09: Sustained Ocean Observations and Information for Society" Conference, edited by J. Hall, D. E. Harrison, and
785 D. Stammer, ESA Publ. WPP-306, Venice, Italy, 21–25 Sep., 2010.

786 Clegg, M. R., Gaedke, U., Boehrer, B. and Spijkerman, E.: Complementary ecophysiological strategies combine to
787 facilitate survival in the hostile conditions of a deep chlorophyll maximum, *Oecologia*, 169(3), 609–622,
788 doi:10.1007/s00442-011-2225-4, 2012.

789 Cleveland, J. S., Perry, M. J., Kiefer, D. A. and Talbot, M. C.: Maximal quantum yield of photosynthesis in the
790 northwest Sargasso Sea., *Journal of Marine Research*, 47(4), 869–886., 1989.

791 Cloern, J. E.: The relative importance of light and nutrient limitation of phytoplankton growth: A simple index of
792 coastal ecosystem sensitivity to nutrient enrichment, *Aquatic Ecology*, 33(1), 3–16, doi:10.1023/A:1009952125558, 1999.

793 Cloern, J. E., Grenz, C. and Videgar-Lucas, L.: An empirical model of the phytoplankton chlorophyll: carbon ration-
794 the conversion factor between productivity and growth rate., *Limnology and Oceanography*, 40(7), 1313–1321, 1995.

795 Crombet, Y., Leblanc, K., Queguiner, B., Moutin, T., Rimmelin, P., Ras, J., Claustre, H., Leblond, N., Oriol, L. and
796 Pujo-Pay, M.: Deep silicon maxima in the stratified oligotrophic Mediterranean Sea, *Biogeosciences*, 8(2), 459–475,
797 doi:10.5194/bg-8-459-2011, 2011.

798 Cullen, J. J.: The Deep Chlorophyll Maximum: Comparing Vertical Profiles of Chlorophyll *a*, *Canadian Journal of*
799 *Fisheries and Aquatic Sciences*, 39(5), 791–803, doi:10.1139/f82-108, 1982.

800 Cullen, J. J. and Eppley, R. W.: Chlorophyll Maximum Layers of the Southern-California Bight and Possible
801 Mechanisms of their Formation and Maintenance, *Oceanologica Acta*, 4(1), 23–32, 1981.

802 D’Ortenzio, F. and D’Alcalà, M. R.: On the trophic regimes of the Mediterranean Sea: A satellite analysis,
803 *Biogeosciences*, 6(2), 139–148, doi:10.5194/bg-6-139-2009, 2009.

804 D’Ortenzio, F., Lavigne, H., Besson, F., Claustre, H., Coppola, L., Garcia, N., Laës-Huon, A., Le Reste, S., Malardé,
805 D., Migon, C., Morin, P., Mortier, L., Poteau, A., Prieur, L., Raimbault, P. and Testor, P.: Observing mixed layer depth,
806 nitrate and chlorophyll concentrations in the northwestern Mediterranean: A combined satellite and NO₃ profiling floats
807 experiment, *Geophysical Research Letters*, 41, 6443–6451, doi:10.1002/2014GL061020, 2014.

808 Dall’Olmo, G. and Mork, K. A.: Carbon export by small particles in the Norwegian Sea, *Geophysical Research*
809 *Letters*, 41(8), 2921–2927, doi:10.1002/2014GL059244, 2014.

810 Dubinsky, Z. and Stambler, N.: Photoacclimation processes in phytoplankton: Mechanisms, consequences, and
811 applications, *Aquatic Microbial Ecology*, 56(2–3), 163–176, doi:10.3354/ame01345, 2009.

812 Dugdale, R. C. and Wilkerson, F. P.: Nutrient sources and primary production in the Eastern Mediterranean, in
813 *Oceanologica Acta*, edited by H. J. Minas and P. Nival, pp. 179–184., 1988.

814 Estrada, M., Marrasé, C., Latasa, M., Berdalet, E., Delgado, M. and Riera, T.: Variability of deep chlorophyll
815 maximum in the Northwestern Mediterranean, *Marine Ecology Progress Series*, 92, 289–300, doi:10.3354/meps092289,
816 1993.

817 Falkowski, P. G. and Laroche, J.: Acclimation to spectral irradiance in algae, *Journal of Phycology*, 27(1), 8–14,
818 doi:10.1111/j.0022-3646.1991.00008.x, 1991.

819 Falkowski, P. G., Dubinsky, Z. and Wyman, K.: Growth-irradiance relationships in phytoplankton, *Limnol.*
820 *Oceanogr.*, 30(2), 311–321, 1985.

821 Fasham, M. J. R., Platt, T., Irwin, B. and Jones, K.: Factors affecting the spatial pattern of the deep chlorophyll
822 maximum in the region of the Azores front, *Progress in Oceanography*, 14(C), 129–165, doi:10.1016/0079-6611(85)90009-6,
823 1985.

824 Fennel, K. and Boss, E.: Subsurface maxima of phytoplankton and chlorophyll: Steady-state solutions from a simple

825 model, *Limnology and Oceanography*, 48(4), 1521–1534, doi:10.4319/lo.2003.48.4.1521, 2003.

826 Flory, E. N., Hill, P. S., Milligan, T. G. and Grant, J.: The relationship between flocculation area and backscatter during a
827 spring phytoplankton bloom, *Deep Sea Research Part I: Oceanographic Research Papers*, 51(2), 213–223,
828 doi:10.1016/j.dsr.2003.09.012, 2004.

829 Furuya, K.: Subsurface chlorophyll maximum in the tropical and subtropical western Pacific Ocean: Vertical profiles
830 of phytoplankton biomass and its relationship with chlorophyll *a* and particulate organic carbon, *Marine Biology*, 107, 529–
831 539, doi:10.1007/bf01313438, 1990.

832 Gačić, M., Civitarese, G., Miserocchi, S., Cardin, V., Crise, A. and Mauri, E.: The open-ocean convection in the
833 Southern Adriatic: A controlling mechanism of the spring phytoplankton bloom, *Continental Shelf Research*, 22(14), 1897–
834 1908, doi:10.1016/S0278-4343(02)00050-X, 2002.

835 Garczarek, L., Dufresne, A., Rousvoal, S., West, N. J., Mazard, S., Marie, D., Claustre, H., Raimbault, P., Post, A. F.,
836 Scanlan, D. J. and Partensky, F.: High vertical and low horizontal diversity of *Prochlorococcus* ecotypes in the Mediterranean
837 Sea in summer, *FEMS Microbiology Ecology*, 60(2), 189–206, doi:10.1111/j.1574-6941.2007.00297.x, 2007.

838 Gardner, W. D., Richardson, M. J. and Smith, W. O.: Seasonal patterns of water column particulate organic carbon
839 and fluxes in the Ross Sea, Antarctica, *Deep Sea Research Part II: Topical Studies in Oceanography*, 47, 3423–3449,
840 doi:10.1016/S0967-0645(00)00074-6, 2000.

841 Geider, R. J.: Light and temperature dependence of the carbon to chlorophyll *a* ratio in microalgae and cyanobacteria:
842 Implications for physiology and growth of phytoplankton, *New Phytologist*, 106(1), 1–34, 1987.

843 Geider, R. J.: Quantitative phytoplankton physiology: implications for primary production and phytoplankton growth,
844 *ICES Marine Science Symposium*, 197, 52–62, 1993.

845 Geider, R. J., MacIntyre, H. L. and Kana, T. M.: Dynamic model of phytoplankton growth and acclimation:
846 Responses of the balanced growth rate and the chlorophyll *a*:carbon ratio to light, nutrient-limitation and temperature, *Marine*
847 *Ecology Progress Series*, 148(1–3), 187–200, doi:10.3354/meps148187, 1997.

848 Golub, G. H. and Van Loan, C. F.: *Matrix Computations*, The Johns., Baltimore and London., 1996.

849 Gong, X., Jiang, W., Wang, L., Gao, H., Boss, E., Yao, X., Kao, S. J. and Shi, J.: Analytical solution of the nitracline
850 with the evolution of subsurface chlorophyll maximum in stratified water columns, *Biogeosciences*, 14(9), 2371–2386,
851 doi:10.5194/bg-14-2371-2017, 2017.

852 Gordon, H. R. and McCluney, W. R.: Estimation of the Depth of Sunlight Penetration in the Sea for Remote Sensing,
853 *Applied Optics*, 14(2), 413–416, doi:10.1364/AO.14.000413, 1975.

854 Gutiérrez-Rodríguez, A., Latasa, M., Estrada, M., Vidal, M. and Marrasé, C.: Carbon fluxes through major

855 phytoplankton groups during the spring bloom and post-bloom in the Northwestern Mediterranean Sea, *Deep Sea Research*
856 Part I: Oceanographic Research Papers, 57(4), 486–500, doi:10.1016/j.dsr.2009.12.013, 2010.

857 Hickman, A. E., Moore, C. M., Sharples, J., Lucas, M. I., Tilstone, G. H., Krivtsov, V. and Holligan, P. M.: Primary
858 production and nitrate uptake within the seasonal thermocline of a stratified shelf sea, *Marine Ecology Progress Series*, 463,
859 39–57, doi:10.3354/meps09836, 2012.

860 Hill, V. J., Matrai, P. A., Olson, E., Suttles, S., Steele, M., Codispoti, L. A. and Zimmerman, R. C.: Synthesis of
861 integrated primary production in the Arctic Ocean: II. In situ and remotely sensed estimates, *Progress in Oceanography*, 110,
862 107–125, doi:10.1016/j.pocean.2012.11.005, 2013.

863 Hodges, B. A. and Rudnick, D. L.: Simple models of steady deep maxima in chlorophyll and biomass, *Deep-Sea*
864 *Research Part I: Oceanographic Research Papers*, 51(8), 999–1015, doi:10.1016/j.dsr.2004.02.009, 2004.

865 Holm-Hansen, O. and Hewes, C. D.: Deep chlorophyll *a* maxima (DCMs) in Antarctic waters: I. Relationships
866 between DCMs and the physical, chemical, and optical conditions in the upper water column, *Polar Biology*, 27(11), 699–
867 710, doi:10.1007/s00300-004-0641-1, 2004.

868 Huot, Y., Babin, M., Bruyant, F., Grob, C., Twardowski, M. S., Claustre, H. and To, C.: Relationship between
869 photosynthetic parameters and different proxies of phytoplankton biomass in the subtropical ocean, *Biogeosciences*, 4(5),
870 853–868, doi:10.5194/bg-4-853-2007, 2007.

871 Ignatiades, L., Psarra, S., Zervakis, V., Pagou, K., Souvermezoglou, E., Assimakopoulou, G. and Gotsis-Skretas, O.:
872 Phytoplankton size-based dynamics in the Aegean Sea (Eastern Mediterranean), *Journal of Marine Systems*, 36(1–2), 11–28,
873 doi:10.1016/S0924-7963(02)00132-X, 2002.

874 Johnson, K. and Claustre, H.: Bringing Biogeochemistry into the Argo Age, *Eos*, 1–7, doi:10.1029/2016EO062427,
875 2016.

876 Johnson, K., Berelson, W., Boss, E., Chase, Z., Claustre, H., Emerson, S., Gruber, N., Körtzinger, A., Perry, M. J.
877 and Riser, S.: Observing Biogeochemical Cycles at Global Scales with Profiling Floats and Gliders: Prospects for a Global
878 Array, *Oceanography*, 22(3), 216–225, doi:10.5670/oceanog.2009.81, 2009.

879 Johnson, K. S. and Coletti, L. J.: In situ ultraviolet spectrophotometry for high resolution and long-term monitoring
880 of nitrate, bromide and bisulfide in the ocean, *Deep-Sea Research Part I: Oceanographic Research Papers*, 49(7), 1291–1305,
881 doi:10.1016/S0967-0637(02)00020-1, 2002.

882 Johnson, K. S., Plant, J. N., Coletti, L. J., Jannasch, H. W., Sakamoto, C. M., Riser, S. C., Swift, D. D., Williams, N.
883 L., Boss, E., Haëntjens, N., Talley, L. D. and Sarmiento, J. L.: Biogeochemical sensor performance in the SOCCOM
884 profiling float array, *Journal of Geophysical Research: Oceans*, 122(8), 6416–6436, doi:10.1002/2017JC012838, 2017.

885 Kiefer, D. A., Olson, R. J. and Holm-Hansen, O.: Another look at the nitrite and chlorophyll maxima in the central

886 North Pacific, *Deep-Sea Research and Oceanographic Abstracts*, 23(12), 1199–1208, doi:10.1016/0011-7471(76)90895-0,
887 1976.

888 Kimor, B., Berman, T. and Schneller, A.: Phytoplankton assemblages in the deep chlorophyll maximum layers off the
889 Mediterranean coast of Israel, *Journal of Plankton Research*, 34(11), 433–443, doi:10.1016/0198-0254(87)90913-7, 1987.

890 Klausmeier, C. a. and Litchman, E.: Algal games: The vertical distribution of phytoplankton in poorly mixed water
891 columns, *Limnology and Oceanography*, 46(8), 1998–2007, doi:10.4319/lo.2001.46.8.1998, 2001.

892 Krom, M. D., Kress, N., Brenner, S. and Gordon, L. I.: Phosphorus Limitation of Primary Productivity in the Eastern
893 Mediterranean-Sea, *Limnology and Oceanography*, 36(3), 424–432, doi:10.4319/lo.1991.36.3.0424, 1991.

894 Krom, M. D., Emeis, K. C. and Van Cappellen, P.: Why is the Eastern Mediterranean phosphorus limited?, *Progress*
895 *in Oceanography*, 85(3–4), 236–244, doi:10.1016/j.pocean.2010.03.003, 2010.

896 Lacour, L., Ardyna, M., Stec, K. F., Claustre, H., Prieur, L., Poteau, A., Ribera D’Alcala, M. and Iudicone, D.:
897 Unexpected winter phytoplankton blooms in the North Atlantic subpolar gyre, *Nature Geoscience*, 10(11), 836–839,
898 doi:10.1038/NGEO3035, 2017.

899 Latasa, M., Gutiérrez-rodríguez, A., Cabello, A. M. and Scharek, R.: Influence of light and nutrients on the vertical
900 distribution of marine phytoplankton groups in the deep chlorophyll maximum, *Planet Ocean*, 80(S1), 57–62,
901 doi:10.3989/scimar.04316.01A, 2016.

902 Lavigne, H., D’Ortenzio, F., Migon, C., Claustre, H., Testor, P., D’Alcalà, M. R., Lavezza, R., Houpert, L. and
903 Prieur, L.: Enhancing the comprehension of mixed layer depth control on the Mediterranean phytoplankton phenology,
904 *Journal of Geophysical Research: Oceans*, 118(7), 3416–3430, doi:10.1002/jgrc.20251, 2013.

905 Lavigne, H., D’Ortenzio, F., Ribera D’Alcalà, M., Claustre, H., Sauzède, R. and Gacic, M.: On the vertical
906 distribution of the chlorophyll *a* concentration in the Mediterranean Sea: a basin scale and seasonal approach,
907 *Biogeosciences*, 12(5), 4139–4181, doi:10.5194/bgd-12-4139-2015, 2015.

908 Leblanc, K., Quéguiner, B., Diaz, F., Cornet, V., Michel-Rodriguez, M., Durrieu de Madron, X., Bowler, C.,
909 Malviya, S., Thyssen, M., Grégori, G., Rembauville, M., Grosso, O., Poulain, J., de Vargas, C., Pujo-Pay, M. and Conan, P.:
910 Nanoplanktonic diatoms are globally overlooked but play a role in spring blooms and carbon export, *Nature*
911 *Communications*, 9(1), 953, doi:10.1038/s41467-018-03376-9, 2018.

912 Letelier, R. M., Karl, D. M., Abbott, M. R. and Bidigare, R. R.: Light driven seasonal patterns of chlorophyll and
913 nitrate in the lower euphotic zone of the North Pacific Subtropical Gyre, *Limnology and Oceanography*, 49(2), 508–519,
914 doi:10.4319/lo.2004.49.2.0508, 2004.

915 Lewis, M. R., Cullen, J. J. and Platt, T.: Phytoplankton and thermal structure in the upper ocean: Consequences of
916 nonuniformity in chlorophyll profile, *Journal of Geophysical Research: Oceans*, 88(C4), 2565–2570,

917 doi:10.1029/JC088iC04p02565, 1983.

918 Li, Q. P. and Hansell, D. A.: Mechanisms controlling vertical variability of subsurface chlorophyll maxima in a
919 mode-water eddy, *Journal of Marine Research*, 74(3), 175–199, doi:10.1357/002224016819594827, 2016.

920 Loisel, H. and Morel, A.: Light scattering and chlorophyll concentration in case 1 waters: A reexamination,
921 *Limnology and Oceanography*, 43(5), 847–858, doi:10.4319/lo.1998.43.5.0847, 1998.

922 Longhurst, A. R. and Glen Harrison, W.: The biological pump: Profiles of plankton production and consumption in
923 the upper ocean, *Progress in Oceanography*, 22(1), 47–123, doi:10.1016/0079-6611(89)90010-4, 1989.

924 Marty, J. C., Chiavérini, J., Pizay, M. D. and Avril, B.: Seasonal and interannual dynamics of nutrients and
925 phytoplankton pigments in the western Mediterranean Sea at the DYFAMED time-series station (1991-1999), *Deep-Sea
926 Research Part II: Topical Studies in Oceanography*, 49(11), 1965–1985, doi:10.1016/S0967-0645(02)00022-X, 2002.

927 Marty, J. C., Garcia, N. and Raimbault, P.: Phytoplankton dynamics and primary production under late summer
928 conditions in the NW Mediterranean Sea, *Deep-Sea Research Part I: Oceanographic Research Papers*, 55(9), 1131–1149,
929 doi:10.1016/j.dsr.2008.05.001, 2008.

930 Mayot, N., D’Ortenzio, F., Uitz, J., Gentili, B., Ras, J., Vellucci, V., Golbol, M., Antoine, D. and Claustre, H.:
931 Influence of the phytoplankton community structure on the spring and annual primary production in the Northwestern
932 Mediterranean Sea, *Journal of Geophysical Research: Oceans*, 122, 1–17, doi:10.1002/2016JC012668, 2017a.

933 Mayot, N., D’Ortenzio, F., Taillandier, V., Prieur, L., Pasqueron de Fommervault, O., Claustre, H., Bosse, A., Testor,
934 P. and Conan, P.: Physical and biogeochemical controls of the phytoplankton blooms in North-Western Mediterranean Sea:
935 A multiplatform approach over a complete annual cycle (2012-2013 DEWEX experiment), *Journal of Geophysical Research:
936 Oceans*, 122, doi:10.1002/2016JC012052, 2017b.

937 Mignot, a., Claustre, H., D’Ortenzio, F., Xing, X., Poteau, a. and Ras, J.: From the shape of the vertical profile of in
938 vivo fluorescence to Chlorophyll *a* concentration, *Biogeosciences*, 8(8), 2391–2406, doi:10.5194/bg-8-2391-2011, 2011.

939 Mignot, A., Claustre, H., Uitz, J., Poteau, A., D’Ortenzio, F. and Xing, X.: Understanding the seasonal dynamics of
940 phytoplankton biomass and the deep chlorophyll maximum in oligotrophic environments: A Bio-Argo float investigation,
941 *Global Biogeochemical Cycles*, 28(8), 1–21, doi:10.1002/2013GB004781., 2014.

942 Mignot, A., Ferrari, R. and Claustre, H.: Floats with bio-optical sensors reveal what processes trigger the North
943 Atlantic bloom, *Nature Communications*, 9(1), 190, doi:10.1038/s41467-017-02143-6, 2018.

944 Mikaelyan, A. S. and Belyaeva, G. A.: Chlorophyll *a* content in cells of Antarctic phytoplankton, *Polar Biology*,
945 15(6), 437–445, doi:10.1007/BF00239721, 1995.

946 Millot, C.: Circulation in the Western Mediterranean Sea, *Journal of Marine Systems*, 20(1–4), 423–442,

947 doi:10.1016/S0924-7963(98)00078-5, 1999.

948 Moore, L. R. and Chisholm, S. W.: Photophysiology of the marine cyanobacterium *Prochlorococcus*: Ecotypic
949 differences among cultured isolates, *Limnology and Oceanography*, 44(3), 628–638, doi:10.4319/lo.1999.44.3.0628, 1999.

950 Morel, A. and Ahn, Y.: Optics of heterotrophic nanoflagellates and ciliates: A tentative assessment of their scattering
951 role in oceanic waters compared to those of bacterial and algal cells, *Journal of Marine Research*, 49(1), 177–202, 1991.

952 Morel, A. and André, J.-M.: Pigment distribution and Primary Production in the Western Mediterranean as Derived
953 and Modeled From Coastal Zone Color Scanner Observations, *Journal of Geophysical Research*, 96(C7), 12685–12698,
954 doi:10.1029/91JC00788, 1991.

955 Morel, A. and Berthon, J.-F.: Surface pigments, algal biomass profiles, and potential production of the euphotic layer:
956 Relationships reinvestigated in view of remote-sensing applications, *Limnology and Oceanography*, 34(8), 1545–1562,
957 doi:10.4319/lo.1989.34.8.1545, 1989.

958 Morel, A. and Bricaud, A.: Inherent optical properties of algal cells including picoplankton: theoretical and
959 experimental results, *Canadian Bulletin of Fisheries and Aquatic Science*, 214, 521–559, 1986.

960 Morris, A. W. and Riley, J. P.: The determination of nitrate in sea water, *Analytica Chimica Acta*, 29, 272–279,
961 doi:10.1016/S0003-2670(00)88614-6, 1963.

962 NREL: SOLPOS 2.0 Documentation. Technical Report, 2000.

963 Organelli, E., Claustre, H., Bricaud, A., Schmechtig, C., Poteau, A., Xing, X., Prieur, L., D’Ortenzio, F., Dall’Olmo,
964 G. and Vellucci, V.: A novel near real-time quality-control procedure for radiometric profiles measured by Bio-Argo floats:
965 protocols and performances, *Journal of Atmospheric and Oceanic Technology*, 33, 937–951, doi:10.1175/JTECH-D-15-
966 0193.1, 2016.

967 Organelli, E., Claustre, H., Bricaud, A., Barbieux, M., Uitz, J., D’Ortenzio, F. and Dall’Olmo, G.: Bio-optical
968 anomalies in the world’s oceans: An investigation on the diffuse attenuation coefficients for downward irradiance derived
969 from Biogeochemical Argo float measurements, *Journal of Geophysical Research - Oceans*, 122, 2017–2033,
970 doi:doi:10.1002/2016JC012629., 2017a.

971 Organelli, E., Barbieux, M., Claustre, H., Schmechtig, C., Poteau, A., Bricaud, A., Boss, E., Briggs, N., Olmo, G. D.,
972 Ortenzio, F. D., Leymarie, E., Mangin, A., Obolensky, G., Penker, C. and Prieur, L.: Two databases derived from BGC-
973 Argo float measurements for marine biogeochemical and bio-optical applications, *Earth System Science Data*, 9, 861–880,
974 doi:https://doi.org/10.5194/essd-9-861-2017, 2017b.

975 Parslow, J. S., Boyd, P. W., Rintoul, S. R. and Griffiths, F. B.: A persistent subsurface chlorophyll maximum in the
976 Interpolar Frontal Zone south of Australia: Seasonal progression and implications for phytoplankton-light-nutrient
977 interactions, *Journal of Geophysical Research: Oceans*, 106(C12), 31543–31557, doi:10.1029/2000JC000322, 2001.

978 Pasqueron de Fommervault, O., D'Ortenzio, F., Mangin, A., Serra, R., Migon, C., Claustre, H., Lavigne, H., Ribera
979 d'Alcala, M., Prieur, L., Taillandier, V., Schmechtig, C., Poteau, A., Leymarie, E., Dufour, A., Besson, F. and Obolensky, G.:
980 Seasonal variability of nutrient concentrations in the Mediterranean Sea: Contribution of Bio-Argo floats, *Journal of*
981 *Geophysical Research: Oceans*, 120, 8528–8550, doi:doi:10.1002/2015JC011103, 2015a.

982 Pasqueron de Fommervault, O., Migon, C., D'Ortenzio, F., Ribera d'Alcalà, M. and Coppola, L.: Temporal
983 variability of nutrient concentrations in the northwestern Mediterranean sea (DYFAMED time-series station), *Deep Sea*
984 *Research Part I: Oceanographic Research Papers*, 100, 1–12, doi:10.1016/j.dsr.2015.02.006, 2015b.

985 Pearson, K.: On lines and planes of closest fit to systems of points in space, *Philosophical Magazine Series 6*, 2(11),
986 559–572, doi:10.1080/14786440109462720, 1901.

987 Perez, V., Fernandez, E., Maranon, E., Moran, X. a. G. and Zubkov, M. V.: Vertical distribution of phytoplankton
988 biomass, production and growth in the Atlantic subtropical gyres, *Deep Sea Res. I*, 53, 1616–1634,
989 doi:10.1016/j.dsr.2006.07.008, 2006.

990 Pollehne, F., Klein, B. and Zeitzschel, B.: Low light adaptation and export production in the deep chlorophyll
991 maximum layer in the northern Indian Ocean, *Deep Sea Research Part II: Topical Studies in Oceanography*, 40(3), 737–752,
992 doi:10.1016/0967-0645(93)90055-R, 1993.

993 Psarra, S., Tselepides, a. and Ignatiades, L.: Primary productivity in the oligotrophic Cretan Sea (NE Mediterranean):
994 seasonal and interannual variability, *Progress in Oceanography*, 46(2–4), 187–204, doi:10.1016/S0079-6611(00)00018-5,
995 2000.

996 Quéguiner, B., Tréguer, P., Peeken, I. and Scharek, R.: Biogeochemical dynamics and the silicon cycle in the Atlantic
997 sector of the Southern Ocean during austral spring 1992, *Deep-Sea Research Part II: Topical Studies in Oceanography*, 44(1–
998 2), 69–89, doi:10.1016/S0967-0645(96)00066-5, 1997.

999 Raimbault, P., Coste, B., Boulhadid, M. and Boudjellal, B.: Origin of high phytoplankton concentration in deep
1000 chlorophyll maximum (DCM) in a frontal region of the Southwestern Mediterranean Sea (algerian current), *Deep-Sea*
1001 *Research Part I*, 40(4), 791–804, doi:10.1016/0967-0637(93)90072-B, 1993.

1002 Roesler, C., Uitz, J., Claustre, H., Boss, E., Xing, X., Organelli, E., Briggs, N., Bricaud, A., Schmechtig, C., Poteau,
1003 A., D'Ortenzio, F., Ras, J., Drapeau, S., Haëntjens, N. and Barbieux, M.: Recommendations for obtaining unbiased
1004 chlorophyll estimates from in situ chlorophyll fluorometers: A global analysis of WET Labs ECO sensors, *Limnology and*
1005 *Oceanography: Methods*, 15(6), 572–585, doi:10.1002/lom3.10185, 2017.

1006 Roesler, C. S. and Barnard, A. H.: Optical proxy for phytoplankton biomass in the absence of photophysiology:
1007 Rethinking the absorption line height, *Methods in Oceanography*, 7, 79–94, doi:10.1016/j.mio.2013.12.003, 2013.

1008 Ryabov, A. B.: Phytoplankton competition in deep biomass maximum, *Theoretical Ecology*, 5(3), 373–385,

1009 doi:10.1007/s12080-012-0158-0, 2012.

1010 Sakamoto, C. M., Johnson, K. S. and Coletti, L. J.: Improved algorithm for the computation of nitrate concentrations
1011 in seawater using an in situ ultraviolet spectrophotometer, *Limnology and Oceanography-Methods*, 7, 132–143,
1012 doi:10.4319/lom.2009.7.132, 2009.

1013 Sakamoto, C. M., Johnson, K. S., Coletti, L. J. and Jannasch, H. W.: Pressure correction for the computation of
1014 nitrate concentrations in seawater using an in situ ultraviolet spectrophotometer, *Limnology and Oceanography: Methods*,
1015 15(10), 897–902, doi:10.1002/lom3.10209, 2017.

1016 Sathyendranath, S., Stuart, V., Nair, A., Oka, K., Nakane, T., Bouman, H., Forget, M. H., Maass, H. and Platt, T.:
1017 Carbon-to-chlorophyll ratio and growth rate of phytoplankton in the sea, *Marine Ecology Progress Series*, 383, 73–84,
1018 doi:10.3354/meps07998, 2009.

1019 Schmechtig, C., Poteau, A., Claustre, H., D’Ortenzio, F. and Boss, E.: Processing Bio-Argo chlorophyll *a*
1020 concentration at the DAC Level, *Argo Data Management*, 1–22, doi:10.13155/39468, 2015.

1021 Schmechtig, C., Thierry, V. and The Bio-Argo Team: Argo Quality Control Manual for Biogeochemical Data, *Argo*
1022 *Data Management*, 1–54, doi:10.13155/40879, 2016a.

1023 Schmechtig, C., Poteau, A., Claustre, H., D’Ortenzio, F., Dall’Olmo, G. and Boss, E.: Processing Bio-Argo particle
1024 backscattering at the DAC level Version, *Argo Data Management*, 1–13, doi:doi:10.13155/39459., 2016b.

1025 Severin, T., Kessouri, F., Rembauville, M., Sánchez-Pérez, E. D., Oriol, L., Caparros, J., Pujo-Pay, M., Ghigliione,
1026 Jean-François D’Ortenzio, F., Taillandier, V., Mayot, N., Durrieu De Madron, X., Ulses, C. and Estournel, Claude2 , Conan,
1027 P.: Open-ocean convection process: a driver of the winter nutrient supply and the spring phytoplankton distribution in the
1028 Northwestern Mediterranean Sea, *Journal of Geophysical Research*, doi:10.1002/2014JC010094, 2017.

1029 Siegel, D. A., Maritorena, S., Nelson, N. B. and Behrenfeld, M. J.: Independence and interdependencies among
1030 global ocean color properties: Reassessing the bio-optical assumption, *Journal of Geophysical Research C: Oceans*, 110(7),
1031 1–14, doi:10.1029/2004JC002527, 2005.

1032 Siokou-Frangou, I., Christaki, U., Mazzocchi, M. G., Montresor, M., Ribera d’Alcalá, M., Vaqué, D. and Zingone,
1033 A.: Plankton in the open Mediterranean Sea: a review, *Biogeosciences*, 7(5), 1543–1586, doi:10.5194/bg-7-1543-2010, 2010.

1034 Stramski, D. and Kiefer, D. A.: Light scattering by microorganisms in the open ocean, *Progress in Oceanography*,
1035 28(4), 343–383, doi:10.1016/0079-6611(91)90032-H, 1991.

1036 Stramski, D., Reynolds, R. A., Kahru, M. and Mitchell, B. G.: Estimation of Particulate Organic Carbon in the Ocean
1037 from Satellite Remote Sensing, *Science*, 285(5425), 239–242, 1999.

1038 Stramski, D., Bricaud, A. and Morel, A.: Modeling the inherent optical properties of the ocean based on the detailed

1039 composition of the planktonic community, *Applied Optics*, 40(18), 2929–2945, doi:10.1364/AO.40.002929, 2001.

1040 Stramski, D., Boss, E., Bogucki, D. and Voss, K. J.: The role of seawater constituents in light backscattering in the
1041 ocean, *Progress in Oceanography*, 61(1), 27–56, doi:10.1016/j.pocean.2004.07.001, 2004.

1042 Taillandier, V., Wagener, T., Ortenzio, F. D., Mayot, N., Legoff, H., Ras, J., Coppola, L., Pasqueron De
1043 Fommervault, O., Diamond, E., Bittig, H., Lefevre, D., Leymarie, E., Poteau, A. and Prieur, L.: Hydrography in the
1044 Mediterranean Sea during a cruise with RV Tethys 2 in May 2015, *Earth System Science Data*, (November), 1–30,
1045 doi:10.17882/51678, 2017.

1046 Tanhua, T., Hainbucher, D., Schroeder, K., Cardin, V., Álvarez, M. and Civitarese, G.: The Mediterranean Sea
1047 system: a review and an introduction to the special issue, *Ocean Science*, 9(5), 789–803, doi:10.5194/os-9-789-2013, 2013.

1048 Tripathy, S. C., Pavithran, S., Sabu, P., Pillai, H. U. K., Dessai, D. R. G. and Anilkumar, N.: Deep chlorophyll
1049 maximum and primary productivity in Indian ocean sector of the southern ocean: Case study in the subtropical and polar
1050 front during austral summer 2011, *Deep Sea Research Part II: Topical Studies in Oceanography*, 118, 240–249,
1051 doi:10.1016/j.dsr2.2015.01.004, 2015.

1052 Uitz, J., Claustre, H., Morel, A. and Hooker, S. B.: Vertical distribution of phytoplankton communities in open ocean:
1053 An assessment based on surface chlorophyll, *Journal of Geophysical Research*, 111(C8005), 1–23,
1054 doi:10.1029/2005JC003207, 2006.

1055 Uitz, J., Claustre, H., Griffiths, F. B., Ras, J., Garcia, N. and Sandroni, V.: A phytoplankton class-specific primary
1056 production model applied to the Kerguelen Islands region (Southern Ocean), *Deep Sea Research Part I: Oceanographic
1057 Research Papers*, 56(4), 541–560, doi:10.1016/j.dsr.2008.11.006, 2009.

1058 Vaillancourt, R. D., Brown, C. W., Guillard, R. R. L. and Balch, W. M.: Light backscattering properties of marine
1059 phytoplankton: relationships to cell size, chemical composition and taxonomy, *Journal of Plankton Research*, 26(2), 191–212,
1060 doi:10.1093/plankt/fbh012, 2004.

1061 Videau, C., Sournia, A., Prieur, L. and Fiala, M.: Phytoplankton and primary production characteristics at selected
1062 sites in the geostrophic Almeria-Oran front system (SW Mediterranean Sea), *Journal of Marine Systems*, 5(3–5), 235–250,
1063 doi:10.1016/0924-7963(94)90049-3, 1994.

1064 Westberry, T. K., Schultz, P., Behrenfeld, M. J., Dunne, J. P., Hiscock, M. R., Maritorena, S., Sarmiento, J. L. and
1065 Siegel, D. A.: Annual cycles of phytoplankton biomass in the subarctic Atlantic and Pacific Ocean, *Global Biogeochemical
1066 Cycles*, 30(2), 175–190, doi:10.1002/2015GB005276., 2016.

1067 Weston, K., Fernand, L., Mills, D. K., Delahunty, R. and Brown, J.: Primary production in the deep chlorophyll
1068 maximum of the central North Sea, *Journal of Plankton Research*, 27(9), 909–922, doi:10.1093/plankt/fbi064, 2005.

1069 Whitmire, A. L., Pegau, W. S., Karp-Boss, L., Boss, E. and Cowles, T. J.: Spectral backscattering properties of

1070 marine phytoplankton cultures, *Optics Express*, 18(14), 15073–15093, doi:10.1029/2003RG000148.D., 2010.

1071 Winn, C. D., Campbell, L., Christian, J. R., Letelier, R. M., Hebel, D. V., Dore, J. E., Fujieki, L. and Karl, D. M.:
1072 Seasonal variability in the phytoplankton community of the North Pacific Subtropical Gyre, *Global Biogeochemical Cycles*,
1073 9(4), 605–620, doi:10.1029/95gb02149, 1995.

1074 Xing, X., Morel, A., Claustre, H., Antoine, D., D’Ortenzio, F., Poteau, A. and Mignot, A.: Combined processing and
1075 mutual interpretation of radiometry and fluorimetry from autonomous profiling Bio-Argo floats: Chlorophyll a retrieval,
1076 *Journal of Geophysical Research*, 116(C06020), 1–14, doi:10.1029/2010JC006899, 2011.

1077 Xing, X., Claustre, H., Blain, S., D’Ortenzio, F., Antoine, D., Ras, J. and Guinet, C.: Quenching correction for in vivo
1078 chlorophyll fluorescence acquired by autonomous platforms: A case study with instrumented elephant seals in the Kerguelen
1079 region (Southern Ocean), *Limnology and Oceanography: Methods*, 10, 483–495, doi:10.4319/lom.2012.10.483, 2012.

1080 Zielinski, O., Voß, D., Saworski, B., Fiedler, B. and Körtzinger, A.: Computation of nitrate concentrations in turbid
1081 coastal waters using an in situ ultraviolet spectrophotometer, *Journal of Sea Research*, 65(4), 456–460,
1082 doi:10.1016/j.seares.2011.04.002, 2011.

1083

1084

1085

1086

1087

1088

1089

1090

1091

1092

1093

1094

1095

1096

1097

Figure captions

1098

1099

1100 **Figure 1:** Geographic location of the multi-variable vertical profiles collected by the BGC-Argo
1101 profiling floats in the Mediterranean Sea. The boundaries of the regions considered in this study are
1102 indicated by the black rectangles. NW, SW and TYR correspond to the Western Basin regions
1103 whereas ION and LEV represent the Eastern Basin regions. The red color indicates BGC-Argo floats
1104 equipped with nitrate sensors. The black color indicates the specific BGC-Argo floats equipped with
1105 nitrate sensors that are used in Figures 10 and 11.

1106

1107 **Figure 2:** Comparison of the nitrate concentrations retrieved from the BGC-Argo floats to the
1108 reference *in situ* measurements. The statistics (determination coefficient and slope) of the regression
1109 analysis between float-derived and *in situ* data are also indicated.

1110

1111 **Figure 3:** Boxplot of the distribution of the chlorophyll *a* concentration (Chl*a*) in the surface (a)
1112 and SCM layers (b), the particulate backscattering coefficient (b_{bp}) in the SCM layer (c), and the depth
1113 (d) and thickness (e) of the SCM for each Mediterranean region considered in this study.

1114

1115 **Figure 4:** Monthly median value of the chlorophyll *a* concentration, Chl*a* (in green) and of the
1116 particulate backscattering coefficient, b_{bp} (in blue) in the SCM layer for the five Mediterranean regions
1117 considered in this study. The annual median of Chl*a* (0.28 mg m^{-3}) and b_{bp} ($5.8 \times 10^{-4} \text{ m}^{-1}$) calculated for
1118 the SCM layer and over the entire Mediterranean Sea are indicated by the green and blue horizontal
1119 lines, respectively. Note the different scales of the y-axes in panels a-e.

1120

1121 **Figure 5:** Monthly median values of the depths of the Subsurface Chl*a* Maximum (in green),
1122 the nitracline (in black), the Subsurface b_{bp} Maximum (in blue), the reference isolume (in yellow) and

1123 the Mixed Layer (in dotted red) for the five Mediterranean regions. The depth of the nitracline is not
1124 shown for the SW as there is no BGC-Argo float equipped with a nitrate sensor for this region.

1125

1126 **Figure 6:** Boxplot of the distribution, for each of the Mediterranean regions considered in this
1127 study, of the difference between the depths of the nitracline $1 \mu\text{M}$ and of the isolume 0.3 mol quanta
1128 $\text{m}^{-2} \text{ d}^{-1}$ (a), of the daily PAR in the SCM layer (b), of the depth (c) and slope (d) of the nitracline, and
1129 the difference between the depths of the nitracline $1 \mu\text{M}$ and of the Mixed Layer Depth (e). The SW is
1130 not always represented, as there is no BGC-Argo float equipped with a nitrate sensor in this region.

1131

1132 **Figure 7:** Normalized vertical profiles of the chlorophyll *a* concentration (Chl*a*) (a, c, e, g, and
1133 i) and particulate backscattering coefficient (b_{bp}) (b, d, f, h, and j) for each of the considered
1134 Mediterranean regions. The Chl*a* and b_{bp} are normalized to their individual profile maximum value,
1135 $\text{Chl}_{a\text{max}}$ and b_{bpmax} , respectively, while the depth is normalized to the euphotic depth (Z_{eu}). The color
1136 code indicates the different types of profiles, namely the different shapes are the “*bloom*”, “*mixed*”,
1137 “*SBM*” (Subsurface Biomass Maximum) with a distinction between the “*SBM_{aZeu}*” and the “*SBM_{bZeu}*”
1138 (for SBM occurring above or below the euphotic depth, respectively), and the “*SCM*” (Subsurface
1139 Chlorophyll Maximum) with a distinction between the “*SCM_{aZeu}*” and the “*SCM_{bZeu}*” (for SCM
1140 occurring or below the euphotic depth, respectively). The black dots indicate the position of the mean
1141 Mixed Layer Depth (MLD) for each type of profile.

1142

1143 **Figure 8:** Monthly occurrence of the different types of profile shapes for each of the five
1144 considered Mediterranean regions. The color code indicates the type of profile shape, namely “*bloom*”,
1145 “*mixed*”, “*SBM*” (Subsurface Biomass Maximum) with a distinction between the “*SBM_{aZeu}*” and the
1146 “*SBM_{bZeu}*” (for SBM occurring above or below the euphotic depth, respectively), and the “*SCM*”
1147 (Subsurface Chlorophyll Maximum) with a distinction between the “*SCM_{aZeu}*” and the “*SCM_{bZeu}*” (for
1148 SCM occurring or below the euphotic depth, respectively).

1149

1150 **Figure 9:** Normalized vertical profiles of the chlorophyll *a* concentration (Chl*a*) (a,c,e, and g)
1151 and particulate backscattering coefficient (b_{bp}) (b,d,f, and h) for each shape type. The Chl*a* and b_{bp} are
1152 normalized to their individual profile maximum value, $Chl_{a_{max}}$ and $b_{bp_{max}}$, respectively, while the
1153 depth is normalized to the euphotic depth (Z_{eu}). The color code and the type of lines indicate the
1154 region of the Mediterranean Sea and the different shapes, respectively. The different shapes are the
1155 “*bloom*”, “*mixed*”, “*SBM*” (Subsurface Biomass Maximum) with a distinction between the “*SBM_{aZeu}*”
1156 and the “*SBM_{bZeu}*” (for SBM occurring above or below the euphotic depth, respectively), and the
1157 “*SCM*” (Subsurface Chlorophyll Maximum) with a distinction between the “*SCM_{aZeu}*” and the
1158 “*SCM_{bZeu}*” (for SCM occurring or below the euphotic depth, respectively). Note the different scales of
1159 the x-axes.

1160

1161 **Figure 10:** Trajectory and Chl*a* time series of the float deployed in the Gulf of Lions (fGL; a-b)
1162 and of the float deployed in the Levantine Sea (fLS; c-d). On panels b and d, the white line shows the
1163 isolume $0.3 \text{ mol quanta m}^{-2} \text{ d}^{-1}$, the blue line indicates the Mixed Layer Depth (MLD) and the black
1164 line the nitracline $1 \mu\text{M}$.

1165

1166 **Figure 11:** Nutrient versus light resource-limitation diagram for the two BGC-Argo floats
1167 deployed in the Gulf of Lions (a) and Levantine Sea (b). The color of the data points indicates the
1168 Chl*a*-to- b_{bp} ratio values. The x- and y-axes respectively represent the PAR and $[\text{NO}_3^-]$ values
1169 normalized to the maximum value calculated over the float lifetime in the layer extending from the
1170 surface to below the SCM. Note that the plots show only data collected within the SCM layer, thus
1171 corresponding to low normalized PAR values (*i.e.* under 25% of the maximum PAR).

1172

1173 **Figure 12:** Schematic representation of the different situations of SCMs in the Mediterranean
1174 Sea during the oligotrophic summer period for the five considered regions of the Mediterranean Sea
1175 along the west-to-east gradient.

1176

1177

1178

1179

1180

1181

1182

1183

1184

1185

1186

1187

1188

1189

1190

1191

1192

1193

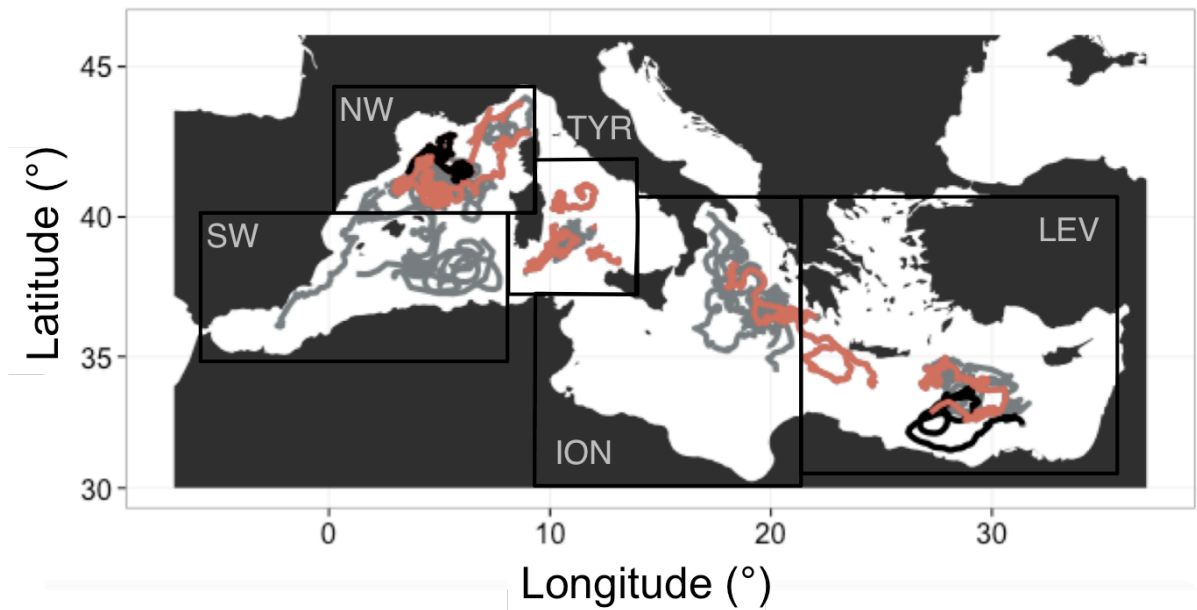
1194

1195 **Table 1:** Regions with the corresponding abbreviation and number of available floats
 1196 and profiles represented in the Mediterranean BGC-Argo database used in the present study
 1197

Region	Basin	Abbreviation	Number of profiles	Number of floats
Gulf of Lions and Ligurian Sea	Western	NW	980	11
Algero-provencal Basin	Western	SW	540	5
Tyrrhenian Sea	Western	TYR	553	5
Ionian Sea	Eastern	ION	936	8
Levantine Sea	Eastern	LEV	1041	7
Total	2	5	4050	36

1198
 1199
 1200
 1201
 1202
 1203
 1204
 1205

1206



1207

1208 **Figure 1:** Geographic location of the multi-variable vertical profiles collected by the BGC-
1209 Argo profiling floats in the Mediterranean Sea. The boundaries of the regions considered in this study
1210 are indicated by the black rectangles. NW, SW and TYR correspond to the Western Basin regions
1211 whereas ION and LEV represent the Eastern Basin regions. The red color indicates BGC-Argo floats
1212 equipped with nitrate sensors. The black color indicates the specific BGC-Argo floats equipped with
1213 nitrate sensors that are used in Figures 10 and 11.

1214

1215

1216

1217

1218

1219

1220

1221
1222
1223
1224
1225
1226
1227
1228
1229
1230
1231
1232
1233
1234
1235
1236
1237
1238
1239
1240
1241
1242
1243

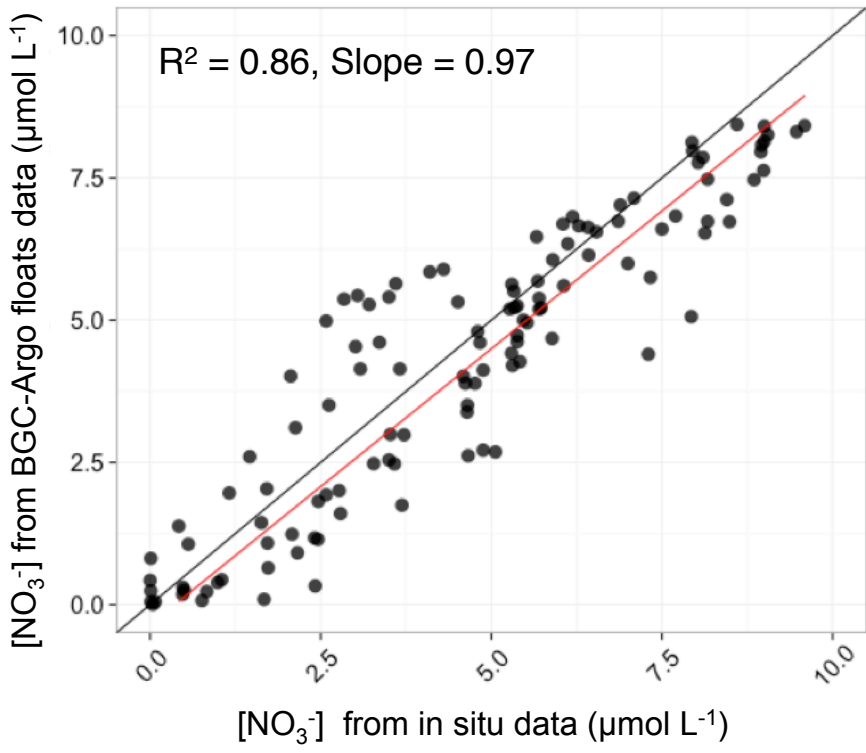
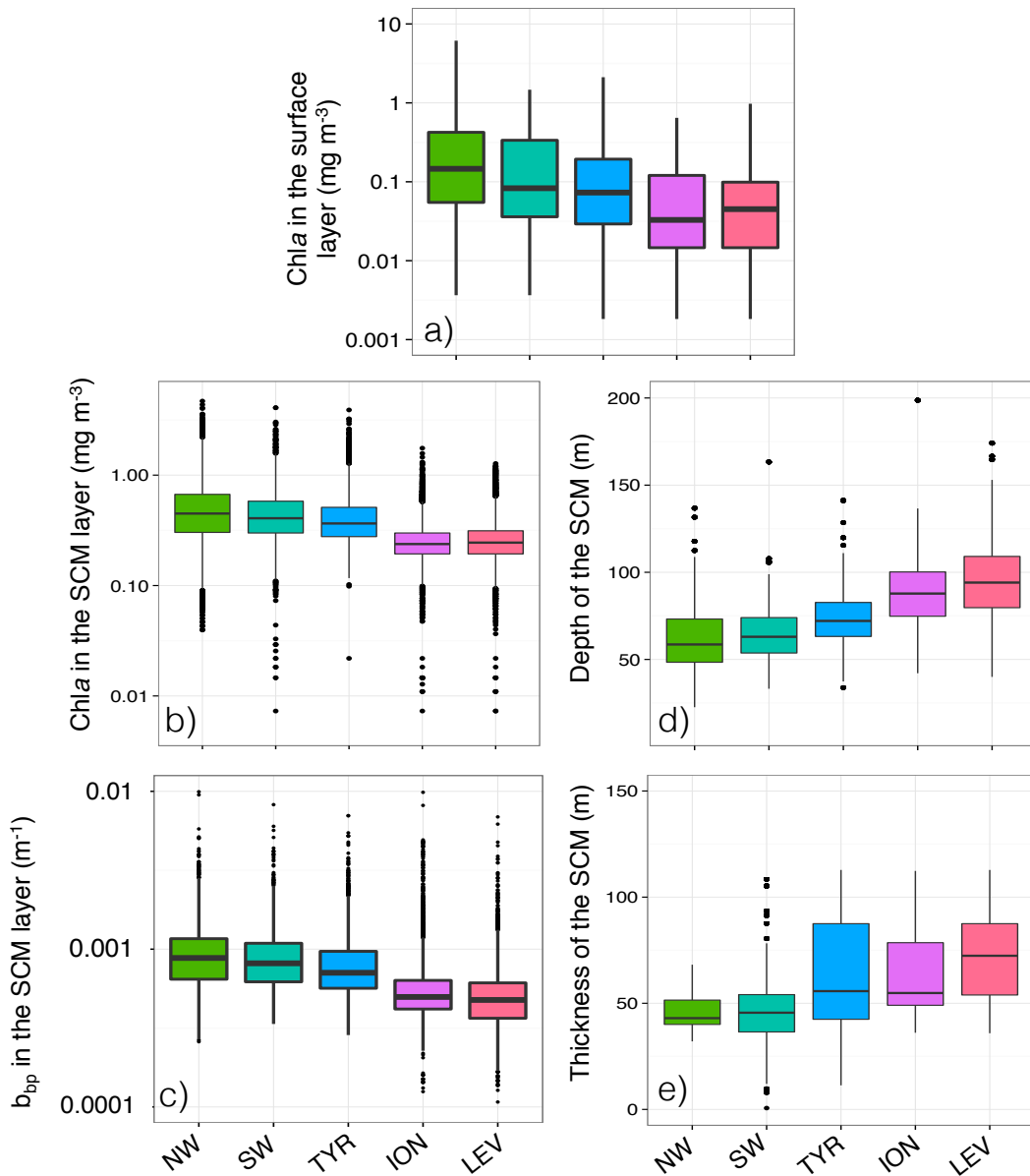


Figure 2: Comparison of the nitrate concentrations retrieved from the BGC-Argo floats to the reference *in situ* measurements. The statistics (determination coefficient and slope) of the regression analysis between float-derived and *in situ* data are also indicated.



1244

1245 **Figure 3:** Boxplot of the distribution of the chlorophyll *a* concentration (Chl*a*) in the surface
 1246 (a) and SCM layers (b), the particulate backscattering coefficient (b_{bp}) in the SCM layer (c), and the
 1247 depth (d) and thickness (e) of the SCM for each Mediterranean region considered in this study.

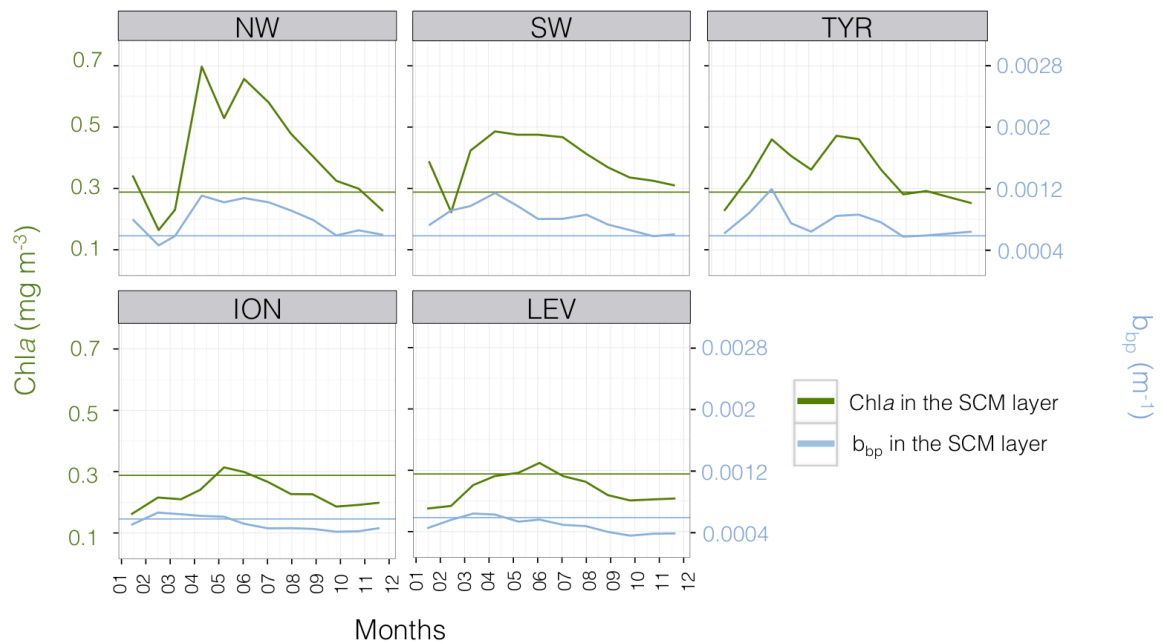
1248

1249

1250

1251

1252



1253

1254 **Figure 4:** Monthly median value of the chlorophyll *a* concentration, Chla (in green) and of the
1255 particulate backscattering coefficient, b_{bp} (in blue) in the SCM layer for the five Mediterranean regions
1256 considered in this study. The annual median of Chla (0.28 mg m⁻³) and b_{bp} (5.8x10⁻⁴ m⁻¹) calculated for
1257 the SCM layer and over the entire Mediterranean Sea are indicated by the green and blue horizontal
1258 lines, respectively. Note the different scales of the y-axes in panels a-e.

1259

1260

1261

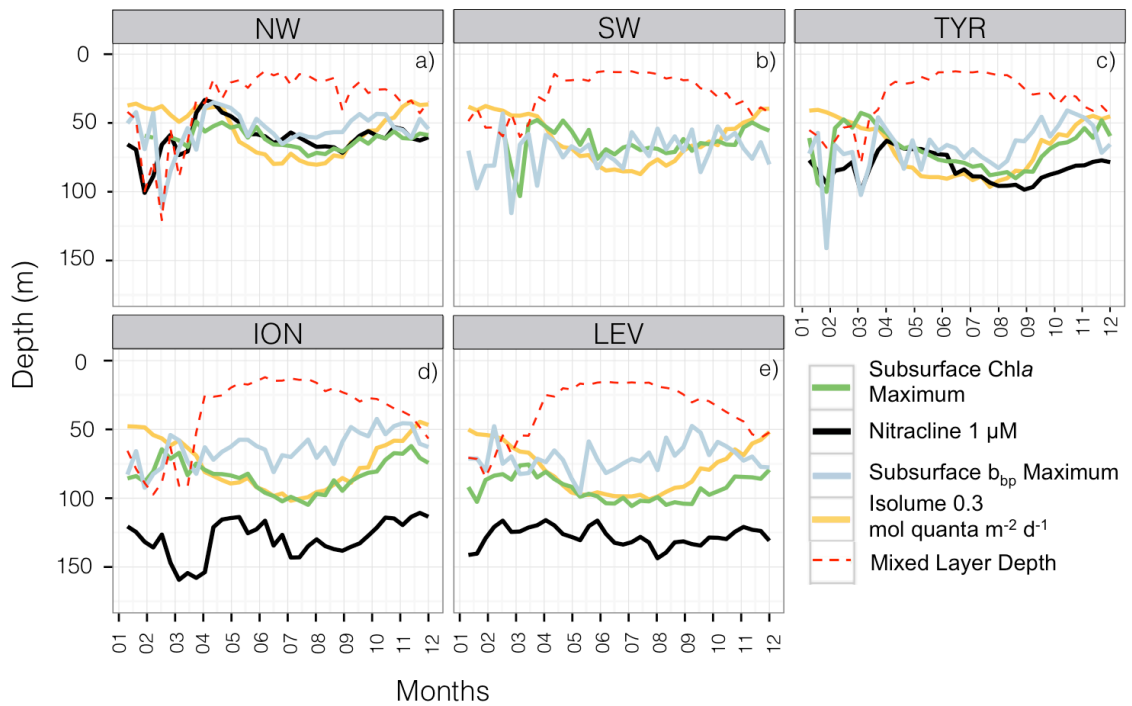
1262

1263

1264

1265

1266



1267

1268 **Figure 5:** Monthly median values of the depths of the Subsurface Chla Maximum (in green),
 1269 the nitracline (in black), the Subsurface b_{bp} Maximum (in blue), the reference isolume (in yellow) and
 1270 the Mixed Layer (in dotted red) for the five Mediterranean regions. The depth of the nitracline is not
 1271 shown for the SW as there is no BGC-Argo float equipped with a nitrate sensor for this region.

1272

1273

1274

1275

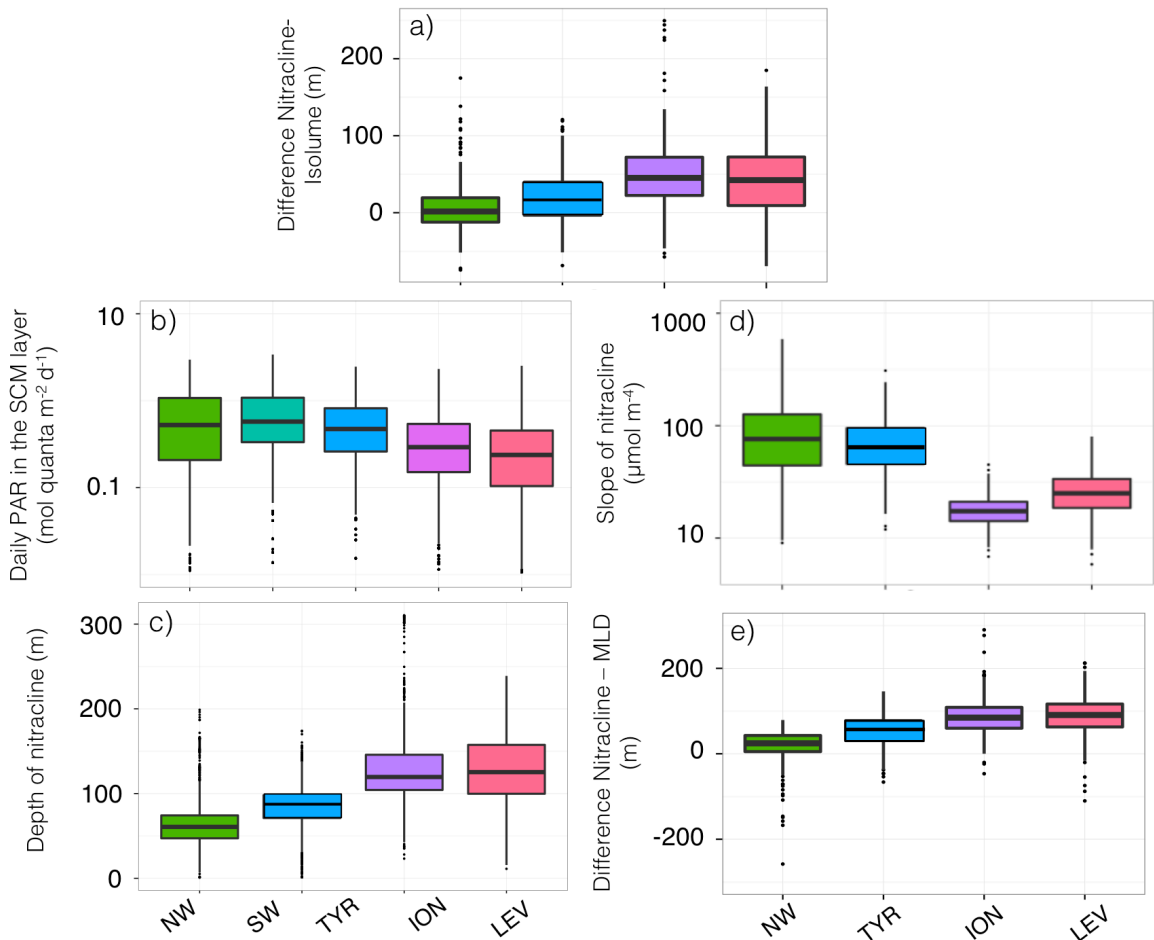
1276

1277

1278

1279

1280



1281

1282 **Figure 6:** Boxplot of the distribution, for each of the Mediterranean regions considered in this
 1283 study, of the difference between the depths of the nitracline 1 μM and of the isolume 0.3 mol quanta
 1284 $\text{m}^{-2} \text{d}^{-1}$ (a), of the daily PAR in the SCM layer (b), of the depth (c) and slope (d) of the nitracline, and
 1285 the difference between the depths of the nitracline 1 μM and of the Mixed Layer Depth (e). The SW is
 1286 not always represented, as there is no BGC-Argo float equipped with a nitrate sensor in this region.

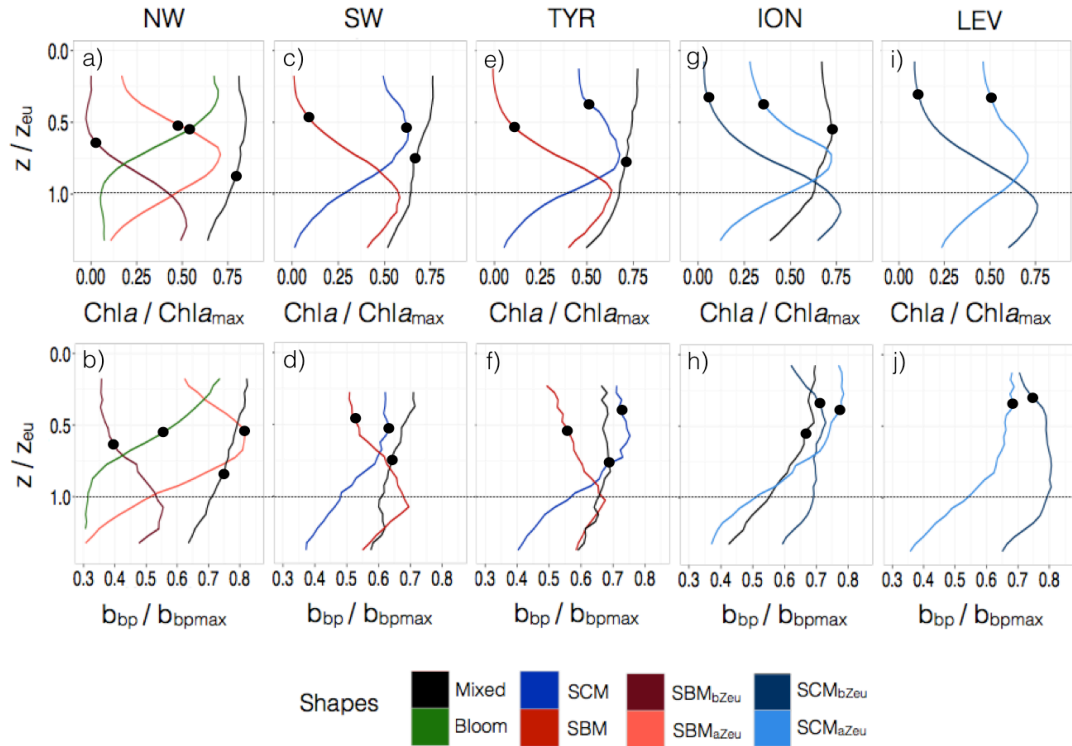
1287

1288

1289

1290

1291



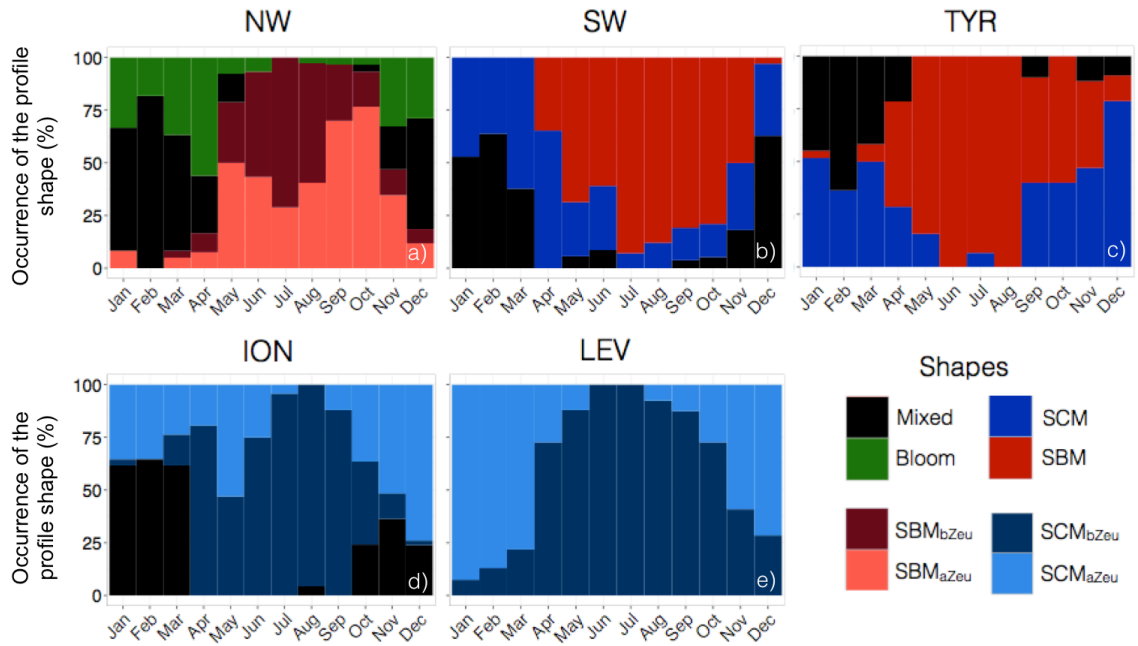
1293

1294 **Figure 7:** Normalized vertical profiles of the chlorophyll *a* concentration (*Chla*) (a, c, e, g, and
 1295 i) and particulate backscattering coefficient (b_{bp}) (b, d, f, h, and j) for each of the considered
 1296 Mediterranean regions. The *Chla* and b_{bp} are normalized to their individual profile maximum value,
 1297 $Chla_{max}$ and b_{bpmax} , respectively, while the depth is normalized to the euphotic depth (Z_{eu}). The color
 1298 code indicates the different types of profiles, namely the different shapes are the “*bloom*”, “*mixed*”,
 1299 “*SBM*” (Subsurface Biomass Maximum) with a distinction between the “*SBM_{aZeU}*” and the “*SBM_{bZeU}*”
 1300 (for *SBM* occurring above or below the euphotic depth, respectively), and the “*SCM*” (Subsurface
 1301 Chlorophyll Maximum) with a distinction between the “*SCM_{aZeU}*” and the “*SCM_{bZeU}*” (for *SCM*
 1302 occurring or below the euphotic depth, respectively). The black dots indicate the position of the mean
 1303 Mixed Layer Depth (MLD) for each type of profile.

1304

1305

1306



1307

1308

Figure 8: Monthly occurrence of the different types of profile shapes for each of the five

1309

considered Mediterranean regions. The color code indicates the type of profile shape, namely “bloom”,

1310

“mixed”, “SBM” (Subsurface Biomass Maximum) with a distinction between the “SBM_{aZeu}” and the

1311

“SBM_{bZeu}” (for SBM occurring above or below the euphotic depth, respectively), and the “SCM”

1312

(Subsurface Chlorophyll Maximum) with a distinction between the “SCM_{aZeu}” and the “SCM_{bZeu}” (for

1313

SCM occurring or below the euphotic depth, respectively).

1314

1315

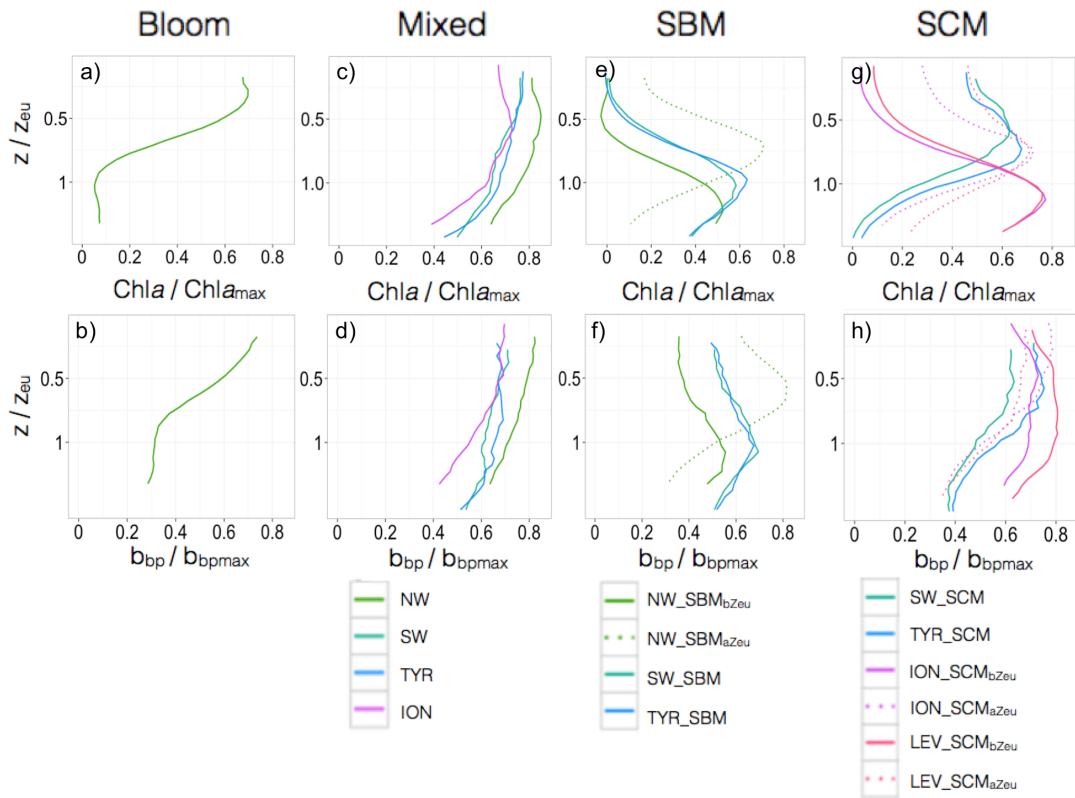
1316

1317

1318

1319

1320



1321

1322

Figure 9: Normalized vertical profiles of the chlorophyll *a* concentration (Chla) (a,c,e, and g)

1323

and particulate backscattering coefficient (b_{bp}) (b,d,f, and h) for each shape type. The Chla and b_{bp} are

1324

normalized to their individual profile maximum value, $Chla_{max}$ and b_{bpmax} , respectively, while the

1325

depth is normalized to the euphotic depth (Z_{eu}). The color code and the type of lines indicate the

1326

region of the Mediterranean Sea and the different shapes, respectively. The different shapes are the

1327

“*bloom*”, “*mixed*”, “*SBM*” (Subsurface Biomass Maximum) with a distinction between the “*SBM_{aZeu}*”

1328

and the “*SBM_{bZeu}*” (for SBM occurring above or below the euphotic depth, respectively), and the

1329

“*SCM*” (Subsurface Chlorophyll Maximum) with a distinction between the “*SCM_{aZeu}*” and the

1330

“*SCM_{bZeu}*” (for SCM occurring or below the euphotic depth, respectively). Note the different scales of

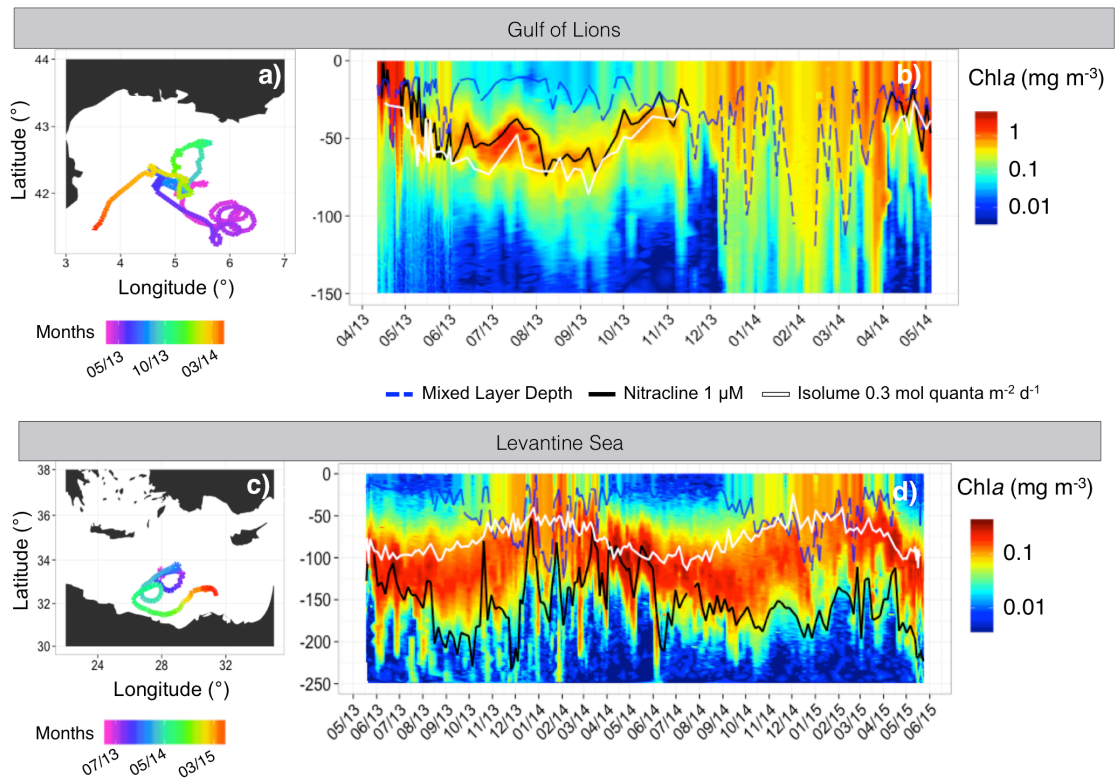
1331

the x-axes.

1332

1333

1334



1335

1336

Figure 10: Trajectory and Chl *a* time series of the float deployed in the Gulf of Lions (fGL; a-

1337

b) and of the float deployed in the Levantine Sea (fLS; c-d). On panels b and d, the white line shows

1338

the isolume $0.3 \text{ mol quanta m}^{-2} \text{ d}^{-1}$, the blue line indicates the Mixed Layer Depth (MLD) and the

1339

black line the nitracline $1 \mu\text{M}$.

1340

1341

1342

1343

1344

1345

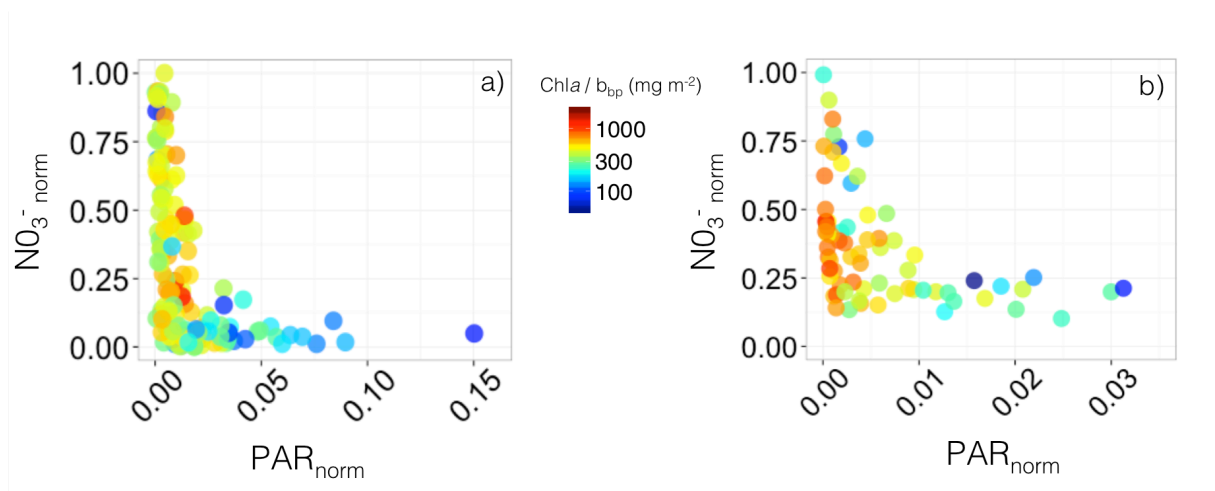
1346

1347

1348

1349

1350



1351

1352 **Figure 11:** Nutrient versus light resource-limitation diagram for the two BGC-Argo floats
1353 deployed in the Gulf of Lions (a) and Levantine Sea (b). The color of the data points indicates the
1354 Chl_a-to-b_{bp} ratio values. The x- and y-axes respectively represent the PAR and [NO₃⁻] values
1355 normalized to the maximum value calculated over the float lifetime in the layer extending from the
1356 surface to below the SCM. Note that the plots show only data collected within the SCM layer, thus
1357 corresponding to low normalized PAR values (*i.e.* under 25% of the maximum PAR).

1358

1359

1360

1361

1362

1363

1364

1365

1366

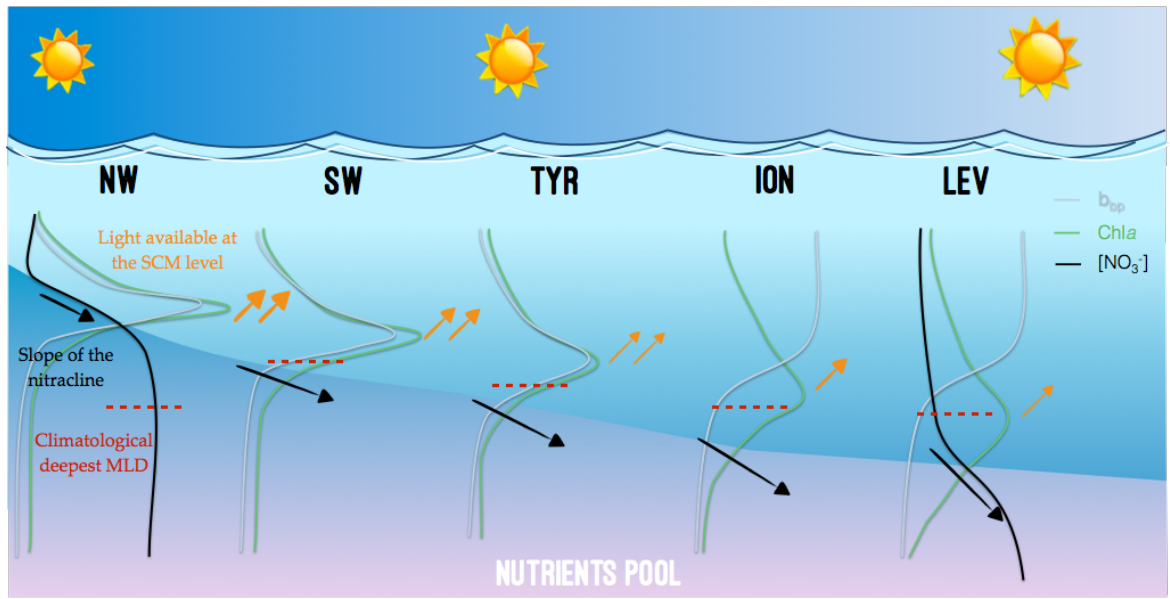
1367

1368

1369

1370

1371



1372
1373

1374 **Figure 12:** Schematic representation of the different situations of SCMs in the Mediterranean
1375 Sea during the oligotrophic summer period for the five considered regions of the Mediterranean Sea
1376 along the west-to-east gradient.

1377
1378